Title: Mutations in Eml1 lead to ectopic progenitors and neuronal heterotopia in mouse and human.

Authors: Kielar M, Tuy FP, Bizzotto S, Lebrand C, de Juan Romero C, Poirier K, Oegema R, Mancini GM, Bahi-Buisson N, Olaso R, Le Moing AG, Boutourlinsky K, Boucher D, Carpentier W, Berquin P, Deleuze JF, Belvindrah R, Borrell V, Welker E, Chelly J, Croquelois A, Francis F

Journal: Nature neuroscience

Year: 2014 Jul

Volume: 17

Issue: 7

Pages: 923-33

DOI: 10.1038/nn.3729

Mutations in Eml1 lead to ectopic progenitors and neuronal heterotopia in mouse and human

Michel Kielar*[1,2], Françoise Phan Dinh Tuy*[3-5], Sara Bizzotto*[3-5], Cécile Lebrand*[2], Camino de Juan[6], Karine Poirier[7], Renske Oegema[8], Grazia Maria Mancini[8], Nadia Bahi-Buisson[9], Robert Olaso[10], Anne Gaelle Le Moing[11], Katia Boutourlinsky[3-5], Dominique Boucher[4,12], Wassila Carpentier[13], Patrick Berquin[11], Jean-François Deleuze[10], Richard Belvindrah[3-5], Victor Borrell[6], Egbert Welker[2], Jamel Chelly[7], Alexandre Croquelois[#1,2], Fiona Francis[#3-5]

1. Department of Clinical Neuroscience, Centre Hospitalier Universitaire Vaudois and University of Lausanne, 1011 Lausanne, Switzerland
2. Department of Fundamental Neurosciences, University of Lausanne, 1005 Lausanne, Switzerland
3. INSERM UMR–S 839, F75005, Paris, France
4. Sorbonne Université, Université Pierre et Marie Curie, F75005, Paris, France
5. Institut du Fer à Moulin, F75005, Paris, France
6. Instituto de Neurociencias, CSIC & Universidad Miguel Hernández, 03550 Sant Joan d'Alacant, Alicante, Spain
7. Inserm U1016, Université René Descartes, Institut Cochin, 75014 Paris, France
8. Department of Clinical Genetics, Erasmus Medical Center, Rotterdam, The Netherlands
9. Hopital Necker Enfants Malades Pediatric Neurology APHP, Université Paris Descartes, 75015 Paris, France
10. CEA/DSV/Institut de Génomique, Centre National de Genotypage, 91057 Evry, France
11. Service de neuropédiatrie, CHU Amiens–Nord, 80054 Amiens cedex 1, France
12. Laboratoire de Biologie du Développement, CNRS UMR 7622, 75252 Paris Cedex 05
13. Plateforme post-génomique de la Pitié–Salpêtrière, Faculty of medicine, 75013, Paris.

* These authors contributed equally to the work.

# These authors jointly directed the project.

SUMMARY

Neuronal migration disorders such as lissencephaly and subcortical band heterotopia are associated with epilepsy and intellectual disability. *DCX*, *PAFAH1B*1 and *TUBA1A* are mutated in these disorders, however corresponding mouse mutants do not show heterotopic neurons in the neocortex. On the other hand, spontaneously arisen *HeCo* mice display this phenotype and our study reveals that misplaced apical progenitors contribute to heterotopia formation. While *HeCo* neurons migrate at the same speed as wild–type, abnormally distributed dividing progenitors were found throughout the cortical wall from E13. We identified *Eml*1, coding for a microtubule–associated protein, as the mutant gene in *HeCo* mice. No full–length transcripts were identified due to a retrotransposon insertion in an intron. *Eml*1 knock–down mimics the *HeCo* progenitor phenotype, and re–expression rescues it. We further show that *EML*1 is mutated in ribbon–like heterotopia in human. Our data link abnormal spindle orientations, ectopic progenitors and severe heterotopia in mouse and human.

Classical subcortical band heterotopia (SBH), part of the type I lissencephaly spectrum, is characterized by the presence of aberrantly localized neurons, in the form of a band in the white matter, below a cortex which appears relatively normal by magnetic resonance imaging (MRI)[1]. The identification of *PAFAH1B1*, *Doublecortin* (*DCX)* and α1–tubulin (*TUBA1A)* genes, coding for microtubule associated proteins and a tubulin isoform, highlights the involvement of microtubule cytoskeletal defects in these neuronal migration disorders[2]. The pathogenesis of subcortical heterotopia (SH) remains little understood, partly because this phenotype has rarely been observed in corresponding mouse models[3-6]. However, acute inactivation of *Dcx* by RNAi in the developing rat cortex[7], and the *tish* rat model with an unknown mutation[8], show SH. Also, *Wnt3a* overexpression in the mouse neocortex[9] and conditional knockouts of *Rapgef*2 and *RhoA*[10,11], as

well as spontaneous *HeCo* and BXD29 mouse mutants[12,13], are characterized by the presence of subcortical heterotopic neurons. We set out to identify how heterotopia arises in *HeCo* brains, and the nature of the corresponding human malformation.

HeCo mice present bilateral masses of heterotopic neurons in the white matter, associated with epilepsy and subtle learning deficits in the adult, thus constituting an interesting genetic model for the pathophysiological study of SH[12]. We show here that *HeCo* developing cortices exhibit a proportion of abnormally distributed dividing cells from early corticogenesis, present in the intermediate zone (IZ) and cortical plate (CP), whilst neuronal locomotion is unaffected. Using whole genome single nucleotide polymorphism (SNP) and transcriptome analyses, we identified a candidate region and the perturbed expression of *Echinoderm microtubule associated protein–like* 1 (*Eml*1) in *HeCo* mice. In human, we also identified mutations in *EML*1 (*EMAPL*) in two families with giant bilateral, ribbon–like heterotopia[14]. This represents the first gene identified for this atypical form of heterotopia. The role of Eml1/EML1 in brain development has not previously been characterized. We show here that Eml1 associates with microtubules and has a cell cycle–dependent localization, becoming enriched in midzone regions of mitotic neuronal progenitors. We identify an increased proportion of oblique mitotic spindle orientations in *HeCo* apical progenitors, which may favor asymmetric inheritance of apical membrane[15]. *Eml*1*/EML*1 is thus a microtubule–binding protein whose disruption leads to ectopic neuronal progenitors, highlighting their role in the pathogenesis of severe forms of heterotopia.

RESULTS

Development of the heterotopia in the *HeCo* cortex

Adult *HeCo* mice present SH in the rostro–medial part of the neocortex close to the hippocampus (**Fig. 1a and Supplementary Fig. 1a**). We examined *HeCo* forebrains at different stages of development. At embryonic day 15 (E15), there was no obvious accumulation of heterotopic

neurons in the *HeCo* IZ[12]. By E17, we found that both early–born Tbr1 positive ($^+$) and late–born Cux1$^+$ neurons formed the heterotopia (**Fig. 1b,c**). Also, Nestin$^+$ radial glial cell (RGC) fibres, the guides for migrating neurons, appeared disorganized locally in heterotopic regions (**Fig. 1b**). At this stage, Tbr1$^+$ neurons were also abundant between the heterotopia and CP, though most wild–type Tbr1$^+$ neurons had finished migrating to form layer VI (**Fig. 1b**).

At P3 in *HeCo*, almost all Tbr1$^+$ neurons had reached their final destination in layer VI above the heterotopia, whereas many Cux1$^+$ neurons had failed to reach cortical layers II/IV and were present in the heterotopia (**Fig. 1d**). Strikingly at this stage, and to a lesser extent at P7 (**Supplementary Fig. 1b**), we observed columns of Cux1$^+$ neurons between the heterotopia and the cortex, while the migration of these neurons was already complete in wild–type (**Fig. 1d**). We found only rare glial cells in the heterotopia postnatally (**Supplementary Fig. 1c,d**), similar to layers II/IV. The heterotopia is thus populated by early–, followed by late–born neurons that subsequently migrate in columns between the heterotopia and the CP, having a temporal delay with respect to wild–type. Some of the last–born neurons remained trapped in the postnatal and adult white matter.

***HeCo* neurons can migrate as well as wild–type cells**

In order to test migration, we performed *ex vivo* electroporation of a pCAG–EGFP reporter plasmid in E15.5 dorsal ventricular zone (VZ) of *HeCo* (n=5) and wild–type (n=3) embryos. EGFP$^+$ migrating neurons were imaged in slices after 3 days *in vitro* (DIV) using video microscopy (**Fig. 2a**). Compared to wild–type, significantly fewer *HeCo* EGFP$^+$ cells reached the CP (**Fig. 2a**, wild–type 77.61 ± 24.29; *HeCo*, 16.11 ± 5.15 10^3/mm^3**,** unpaired *t*–test p=0.0178, 6 degrees of freedom (d.f.), *t*=3.234) although remarkably, motility parameters in the IZ and CP were similar for wild–type and *HeCo* neurons (speed μm/hr, wild–type, 33.09 ± 0.65; *HeCo* 33.77 ± 0.64; unpaired *t*–test: p=0.4535, 6077 d.f., *t*=-0.750; pause frequency, wild–type, 0.314 ± 0.020; *HeCo* 0.309 ± 0.027 pauses/hr; p=0.8836, 167 d.f., *t*=0.147; pause duration, wild–type 30.09 ± 1.62 min; *HeCo* 32.25 ±

1.93 min, p=0.3917, 640 d.f., *t*=-0.857). We found no differences in trajectory orientations of wild–type and mutant neurons (**Fig. 2a,** average angle relative to the VZ, wild–type 135.88° ± 0.96, *HeCo* 136.03° ± 0.97, unpaired *t*–test p=0.9073, 5048 d.f., *t*=-0.116). Furthermore, $EGFP^+$ neurons analyzed in the CP at P3 showed a similar morphology in wild–type and *HeCo* (**Fig. 2b**). While the motility properties and morphogenesis of *HeCo* neurons appear normal, many mutant cells born at E15.5 remain blocked in the lower IZ (**Fig. 2a**).

To further test the ability of *HeCo* neurons to migrate, we performed *in utero* transplantation experiments, injecting labeled E14.5 wild–type or *HeCo* cortical cells in isochronic wild–type mouse brains[11]. At E17.5 we observed no differences in cell distribution in individual zones between the genotypes (**Fig. 2c,** total χ^2–test p=0.177, 4 d.f., χ^2 =6.31). Thus *HeCo* mutant cells in a wild–type environment migrate as efficiently as wild–type cells.

Early corticogenesis progenitor defects in *HeCo* brains

To further investigate the origin of the defects, we assessed proliferating cells in *HeCo* brains. We initially performed pulsed 5–bromo 2–deoxyuridine (BrdU) injections at E15 followed by sacrifice 1 h later. In wild–type, $BrdU^+$ cells were largely restricted to the VZ and subventricular zone (SVZ), whereas in *HeCo* brains they appeared spread throughout the cortical wall (**Fig. 3a**). BrdU injections performed earlier, at E13, with sacrifice after 30 min, gave similar results in *HeCo* brains, with $BrdU^+$ cells labeled with Ki–67 (a marker of proliferation) extending outside the proliferative zones, in the IZ and CP (**Fig. 3b**). Thus, early in cortical development, during $Tbr1^+$ cell neurogenesis, there is an altered distribution of *HeCo* progenitors.

To characterize the progression of progenitors through the cell cycle, we determined their labeling index at 30 min (percentage of $Ki\text{-}67^+$ cells also labeled with BrdU)[16]. This was significantly higher in *HeCo*, notably in cells in the IZ and CP (**Fig. 3c,** left), indicating that a higher proportion of cells take up BrdU, either due to a longer S–phase and/or a decreased cell cycle

length. Analysis of embryos sacrificed 24 h after BrdU injection showed that the total number of $BrdU^+$ cells was increased in *HeCo*, due to more labeled cells in the VZ, SVZ and IZ (**Fig. 3b** and **Supplementary Fig. 2a**). We found that more *HeCo* cells remained in the cell cycle (quantified by identifying after 24 h those $BrdU^+$ cells which were $Ki–67^+$), particularly in the SVZ, IZ and CP (**Fig. 3c,** right). Misplaced progenitors in E13 *HeCo* brains, present outside the ventricular zones, hence continue to proliferate longer than wild–type cells.

We next investigated whether these defects were still present at late–stages of corticogenesis. At E19, ectopic proliferating cells were also found in *HeCo* IZ and CP, although in lower densities, and mainly positioned around the heterotopia (**Fig. 3d** and **Supplementary Fig. 2b**). Labeling index was also increased in the E19 *HeCo* cortex compared to WT, notably in the IZ and CP and cell cycle exit reduced in all layers (data not shown). Thus, at both early and late stages of corticogenesis, many actively dividing cells are abnormally positioned in *HeCo* brains. This is associated with altered cell death, as increased numbers of $caspase–3^+$ cells were identified in E13 *HeCo* versus wild–type cortices (**Fig. 3e**).

Furthermore, we observed both $Pax6^+$ RGCs and $Tbr2^+$ basal progenitors proliferating in ectopic positions as shown by co–labeling with phospho(Ser10)–histone 3 (PH3, a mitotic marker), and Ki–67 (**Supplementary Fig. 2b,c**). Thus, $Pax6^+$ and $Tbr2^+$ *HeCo* progenitors divide within the IZ and CP.

The *Eml*1 gene is mutated in *HeCo* mice

To identify the perturbed molecular mechanisms leading to ectopic progenitors, we searched for the mutant gene. The mode of inheritance of the *HeCo* phenotype is autosomal recessive[12]. *HeCo* mice were crossed with C57BL/6J wild–type mice. Tail DNAs from C57BL/6J and NOR–CD1 wild–type, as well as NOR–CD1 *HeCo* F0 mice, 31 unaffected heterozygote F1 and 42 affected F2 mice were used to screen an array of 1536 SNP markers covering the mouse genome (MGI accession).

Only one genomic region on chromosome 12 showed 3 adjacent homozygous NOR allele markers in all affected individuals (**Fig. 4a**). Flanking markers (5' rs13481624 and 3' rs3692361), found heterozygote for some affected F2 individuals, defined a 13.7 Mb region (**Supplementary Fig. 3a**).

A list of 96 SNPs within this region, and an additional *HeCo* pedigree, were generated for a second round of genotyping. This allowed fine–mapping of the mutation to a 4.4 Mb region containing 30 annotated genes (**Fig. 4a,** MGI accession and **Supplementary Table 1**). Additional SNPs identified by sequencing coding exons and intron–exon boundaries of 15 genes (**Supplementary Fig. 3a**) allowed a further refinement of the candidate region.

To identify the mutant gene, we also carried out transcriptome microarray experiments (GEO accession GSE56907), comparing wild–type and *HeCo* E18 brain hemisphere total RNAs. Strikingly, an *Eml*1 3'UTR probe mapping to the candidate region on mouse chromosome 12 exhibited a 5.5–fold decrease in fluorescence intensity in mutants, whereas a coding sequence probe (*Eml*1 exon 5, **Fig. 4b**) showed a 1.9 fold increase (n=8 mice/genotype, 3'UTR probe, wild–type, mean fluorescence intensity 428.6 ± 13.1, *HeCo*, 77.5 ± 1.2; unpaired *t*–test 1 d.f., p=0.0001, *t*=708.158; exon 5 probe, wild–type, 79.8 ± 1.2, *HeCo*, 155.0 ± 8.6, p=0.0001, *t*=75.859)). In RT–qPCR analyses (n=7 WT; n=8 *HeCo*; primers in **Supplementary Table 2**), confirming the microarray data, *Eml*1 transcripts containing exons 3 and 4 were 2.5–fold increased in *HeCo* (unpaired *t*–test, 0.992 ± 0.03 *HeCo*, versus 0.398 ± 0.01 wild–type, relative units, p=0.0001, d.f. 1, t=318.374), and full length transcripts containing 3'UTR sequences were decreased more than 96–fold (unpaired *t*–test, 0.00187 ± 0.0002 *HeCo* versus 0.18052 ± 0.003 wild–type, p=0.0001, d.f. 1, t=2569,691). This reduction in expression of full length transcripts, together with the localization of *Eml*1 in the 4.4 Mb genomic region defined by SNP analyses, strongly suggested that *Eml*1 is the mutated gene in *HeCo* mice.

An early retrotransposon in *HeCo* intron 22 of *Eml*1

To investigate mutation mechanisms, we searched for disruptions of *Eml*1 in genomic DNA, and identified abnormalities in intron 22 (**Fig. 4c** and **Supplementary Fig. 3b**). RT–PCRs were performed comparing NOR–CD1 wild–type and *HeCo Eml*1 transcripts from E18 brains (**Supplementary Fig. 3c,d**). We amplified a 420 bp product extending from exon 19 to the 3'UTR from wild–type but not from *HeCo*. A secondary amplification using nested primers revealed two faint smaller *HeCo* bands (**Fig. 4d**), corresponding to skipping of exon 22, or exons 21 and 22. Both abnormal transcripts are predicted to induce a frameshift and premature stop codon in exon 23, leading to the loss of 84 or 117 C terminal amino acids, replaced by 19 or 20 junk amino acids, respectively (Genbank accessions KJ734705–KJ734706).

We amplified intron 22, identifying an expected 910 bp fragment in NOR–CD1 wild–type, whereas a >5 kb fragment was amplified from *HeCo* genomic DNAs (**Fig. 4e** and **Supplementary Fig. 3e**). Sequencing revealed a 5.5 kb early retrotransposon (ETn) element (Genbank KJ734704), flanked by a 6 bp direct repeat in the intron, and highly similar to several ETn type II retrotransposons[17]. Of note, the insertion of an ETn II element giving rise to the *barrelless* mutant was previously described in the same NOR–CD1 stock[18,19]. We identified chimeric *Eml*1–ETn transcripts corresponding to perturbed splicing, premature termination and/or transcription initiation (**Fig. 4f**). Thus, normal full length transcripts are absent in *HeCo* brains, replaced by trace levels of shortened transcripts and by chimeric *Eml*1–ETn transcripts, all leading to truncated *Eml*1 and predicted perturbed protein conformation.

*Eml*1 plays an important role in progenitors

*Eml*1 expression in the brain, previously uncharacterized, was examined by *in situ* hybridization (**Fig. 5a–i**). Mouse *Eml*1 transcripts were detected from E13.5 to P1 in cortical neuronal progenitors of the VZ and post–mitotic neurons of the CP (**Fig. 5a–f** and **Supplementary Fig. 4a–g,j,l**). At E13.5, expression was predominant in progenitor zones, whereas from E14.5 onwards, expression

was also observed in the CP. At E17.5, no further expression was observed in the VZ. No full–length *Eml*1 transcripts were detected by *in situ* hybridization in *HeCo* brains (**Supplementary Fig. 4h–i**). In the adult brain, sparse *Eml*1 labeling persisted in the cortex, hippocampus and thalamus (**Fig. 5g** and **Supplementary Fig. 4m–s**). To investigate progenitor zones more similar to those present in primate brains, we further examined *Eml*1 expression in the brain of a gyrencephalic species, the ferret. At P0, a developmental stage similar to mouse E15, ferret *Eml*1 expression was detected both in the CP and in all proliferative layers (**Fig. 5h,i**), including the outer subventricular zone (OSVZ), which has expanded during evolution[20-23]. These combined data are consistent with the expression of *Eml*1 in different types of neuronal progenitors, as well as in post–mitotic neurons during cortical development.

To further confirm Eml1's role in progenitors related to the *HeCo* phenotype, we performed rescue experiments by re–expressing this gene under the control of the RGC–specific BLBP promoter. *HeCo* mouse brains were electroporated *in utero* with either BLBP–IRES–EGFP or BLBP–Eml1–IRES–EGFP and the positions of RGCs analysed one day later (**Fig. 5j**). Rescue with Eml1 significantly reduced the number of ectopic $EGFP^+$ RGCs in the SVZ/IZ (% cells SVZ/IZ mean=35.11 ± 3.789, versus Ctrl, % cells SVZ/IZ mean=59.37 ± 3.292, unpaired *t*–test p=0.0003, 1 d.f., *t*=23.369). In a knockdown approach, we also inactivated the gene acutely. In N2a cells, a transfected *Eml*1 short hairpin (sh) construct reduced transcript levels by minimally 43 % (relative units, sh_control 1.02 ± 0.127, sh_*Eml*1 0.57 ± 0.051, unpaired *t*–test p=0.008 d.f.=1, t=10.906, 6 qPCR experiments from 2 independent cell transfections per condition). Electroporation of these constructs in E14.5 wild–type mouse brain led at E15.5 to more proliferating RGCs in the sh–SVZ/IZ, and this was rescued by an RGC–specific re–expression of sh–resistant *Eml*1 (**Fig. 5k–m,** Ctrl, % cells SVZ/IZ mean=7.09 ± 1.320, RNAi, % cells SVZ/IZ mean=16.8 ± 2.055, Rescue RNAi, % cells SVZ/IZ mean=6.81 ± 0.931). Thus correct expression of Eml1 in RGCs is critical for their normal distribution.

Eml1 localization and abnormal *HeCo* spindle orientations

EML1 is a member of the EMAP family, containing six members in human (NCBI Unigene database) and originally identified in the sea urchin, in which EMAP represents an abundant microtubule–associated protein[24]. Studies of other EMAP proteins have pointed to roles in cell division, mechanotransduction and sensory function[25-29]. To question Eml1's role in cortical cells, and in the absence of antibodies specifically detecting the endogeneous protein, we first assessed its subcellular localization by transfecting tagged Eml1 in primary cultures of E12.5 mouse cortices. These cultures contain Ki–67^{+} progenitors expressing Pax6 or Tbr2, and post–mitotic neurons expressing Dcx (**Supplementary Fig. 5a**). In neurons, punctate Eml1 appeared distributed throughout the cell, aligning with microtubules, and prominent in perinuclear regions and growth cones (**Supplementary Fig. 5b,c**). No morphology differences were observed in *HeCo* versus wild–type neurons *in vitro* (**Supplementary Fig. 5d,e** and data not shown). In progenitors, a cell cycle–dependent, punctate localization of YFP–EML1 (or Flag–Eml1) was observed (**Fig. 6a** and **Supplementary Fig. 6a–e**), enriched in perinuclear regions in interphase cells and the region of spindle microtubules during metaphase. During telophase and cytokinesis, similar to that described previously for EML3[30], YFP–EML1 labeled puncta were enriched in the midzone area, a region interconnecting the separating cells[31].

RGC morphology is not retained in dissociated cultures, and is crucial for the function of these cells. We hence looked more carefully at native progenitors *in vivo* using a cytoplasmic marker of mitotic progenitors, phospho–vimentin (P–vim) at E13 (**Fig. 6b**). Layer distribution of both Pax6^{+} and Tbr2^{+} cells, double–labeled with P–vim, were abnormal (**Fig. 6c**). Less RGCs in mitosis were apparent at the ventricular lining in *HeCo* brains (**Fig. 6b** and **Supplementary Fig. 2**).

Using β–catenin, which labels adherens junctions between RGCs, we observed an apparently intact ventricle lining in *HeCo* brains at E13 (**Fig. 6d**). A similar result was also revealed

at E16 with Par3, a polarity protein present in RGC apical endfeet, atypical PKC and β–catenin (**Supplementary Fig. 7).** However, while in wild–type brains, most anaphasic cells located at the ventricle lining showed vertically oriented DNA (60–90° angle perpendicular to the ventricular surface)[15] with few oblique and horizontal divisions, the distribution of cleavage orientations was significantly different in *HeCo* at E13 and E16 (**Fig. 6e,** and not shown)**.** Such differences may explain the manner by which $Pax6^+$ ectopic progenitors arise, since oblique cleavage orientations are likely to favor asymmetric inheritance of apical membrane attachments and detachment of progenitors[15]. Eml1 is thus likely to play a critical role in the finely tuned mechanisms regulating spindle orientation and apical RGC attachment.

Mutations in human *EML*1 lead to cortical malformations

Human *EML*1 maps to 14q32, and apart from oncogenic chromosomal rearrangements[32], no other obvious disorders have been linked to this gene (NCBI OMIM database). However, 14q32 telomeric deletions have been associated with intellectual disability[33] and in one girl, lissencephaly was reported[34]. We therefore screened a panel of 47 non–consanguineous and 47 consanguineous sporadic, and 9 familial cortical malformation cases as well as 300 control individuals by PCR (primers in **Supplementary Table 2**). One cortical malformation family (P135) showed compound heterozygote mutations in their three affected children (**Fig. 7a–c**). A c.481C>T nucleotide mutation in exon 5 (sequence accession number NM_004434), changing an arginine residue (p.R138) into a stop codon, was transmitted from the mother, and a c.796A>G mutation in exon 8, changing a threonine into an alanine residue (p.T243A, uncharged polar residue changed to aliphatic non–polar, Provean prediction –4.038 'deleterious', SIFT 0.01 'damaging', Polyphen–2 0.594 'possibly damaging'), was transmitted from the father. In a second family from a different cohort (3489), the proband and an aborted fetus exhibited a homozygote c.673T>C mutation (**Fig. 7a,c** and **Supplementary Fig. 8a**) (p.W225R, hydrophobic non–polar residue changed to highly

basic hydrophilic residue, Provean prediction –12.889 'deleterious', SIFT 0.00 'damaging', Polyphen–2 0.183 'benign'). These changes were not identified in Exome Variant Server, dbSNP and 1000 Genomes databases. The affected children from each family demonstrated similar MRI patterns, combining giant bilateral periventricular and ribbon–like subcortical heterotopia with polymicrogyria and corpus callosum agenesis. The heterotopia was most obvious in frontal regions, extending from the lateral ventricles to the white matter in a convoluted form (**Fig. 7c**). For each child, exhibiting normal height and weight, a head circumference greater than or equal to the 98th percentile (+2.5 SD) was noted from birth (**Supplementary Fig. 8b,c**). Human *EML*1 mutations are thus associated with a severe, atypical form of SH, associated with epilepsy and intellectual disability.

Both human missense mutations target highly conserved residues (chordates and echinoderms) and fall in the Hydrophobic Echinoderm–Like Protein (HELP) domain (**Fig. 7d** and **Supplementary Fig. 9a**), a region characteristic of the EMAP family and potentially contributing to tubulin binding[25,30,35]. To better test their microtubule association, wild–type and T243A Eml1 were transfected in Vero or COS7 cells. Using standard fixation protocols, Flag–tagged and non–tagged wild–type Eml1 showed a predominantly cytoplasmic localization during interphase (**Supplementary Fig. 9b-f**). However, mild detergent extraction of soluble proteins revealed microtubule–associated Eml1 (**Fig. 8a**). Using purified proteins we also showed a direct association of GST–tagged EML1 with microtubules (**Fig. 8b,c**). Depolymerizing microtubules by cold treatment in both transfected and non–transfected cells, resulted in Eml1 no longer showing a fibrillar pattern (**Supplementary Fig. 10a**, 0 min). After restoring the cells to 37°C, wild–type Eml1 was found associated, in the form of puncta, with newly nucleated microtubules in most cells, while the T243A mutant protein showed less co–localisation (**Fig. 8d,e**). Even in cells in which microtubules had not been depolymerized by cold treatment, mutant Eml1 reproducibly appeared less well associated with microtubules (**Supplementary Fig. 10b**). Biochemical microtubule

enrichment comparing cells transfected with wild–type or T243A mutant clones also showed reduced co–sedimented mutant protein (**Fig. 8f,** co–sedimentation, T243A mean=56 ± 5 % compared to WT, unpaired *t*–test 1 d.f., p=0.0009, *t*=79.323). Thus, the T243A mutation affects the microtubule association of Eml1, confirming that cytoskeletal interactions are important for the function of this protein, especially during the division of progenitor cells.

DISCUSSION

We identified here a novel corticogenesis gene associated with severe heterotopia in mouse and human. Patients with compound heterozygote or homozygote mutations in *EML*1 exhibit a ribbon–like SH and callosal agenesis. *HeCo* mice, with a retrotransposon insertion perturbing *Eml*1 expression, show ectopic progenitors, abventricular mitosis and SH. Knockdown of *Eml*1 *in utero* in wild–type mice also mis–positions progenitors away from the VZ. This phenotype is rescued by Eml1 re–expression in RGCs. Our converging data suggest that Eml1/EML1 is essential for retaining progenitors in the proliferative zones and that ectopic progenitors represent the primary defect leading to severe heterotopia. This situation differs from classical forms of band heterotopia, likely to be primarily caused by abnormal neuronal migration, and also from periventricular heterotopia, caused by adherens–junction breakages in the ventricular lining, abnormal neuron production in the VZ and/or abnormal neuronal migration[14,36,37].

In *HeCo* brains, although many neurons are unable to reach the CP, we found that migration speed and parameters of E15–born neurons were unchanged compared to wild–type. E14 *HeCo* neurons can also migrate as wild–type cells when transplanted in wild–type brains. On the other hand, the accumulation of ectopic progenitors with a high labeling index within the *HeCo* IZ from as early as E13, and local neuron production, may represent the primary defect in this model. This dense cell mass in the IZ likely forms a physical barrier for migrating neurons produced in the VZ

and SVZ. This combination of abnormalities is associated with a subtle perturbation of RGC fibers, predicted also to further hinder migration. As the IZ increases in size during corticogenesis, progenitors positioned above the heterotopia may convert into neurons that will reach the CP. Interestingly, Tbr1 and Cux1 labelings show that probably all types of neurons, early to late born, sequentially populate the heterotopia and continue to migrate to the CP, with a temporal delay in comparison with wild–type neurons expressing the same markers. A progressive local production and differentiation of different layer–specific cells within or near the heterotopia may also occur over time. These temporal changes in the heterotopia were not predicted from analyses performed postnatally which suggested primarily an upper–layer neuron phenomenon[12]. At P3 and P7, columns of mutant migrating neurons are still observed and finally only upper layer neurons remain trapped in the heterotopia postnatally. As neurogenesis occurs in a lateral to medial gradient[38], upper layer neurons in medial regions are the most susceptible to remain trapped in the IZ, after the migration period, potentially explaining the rostro–medial position of the heterotopia in *HeCo* mice.

Concerning its role in progenitors, the expression pattern of *Eml*1 suggests similarities to *Pax6*, expressed in RGCs between E13.5 and E16.5[39]. In *Pax*6 mutants, ectopic proliferating RGCs are present in the IZ during the same developmental period as those in *HeCo* mice[40]. Our combined data confirm that, already in the mouse cortex, the IZ constitutes a permissive environment for proliferating cells, as also shown by the identification of rare bRG progenitors in this species[41,42]. Also the environment may have an effect on cell cycle parameters, since more proliferating cells take up BrdU. However, although the labeling index of *HeCo* proliferating cells is increased at E13, total numbers of cells in mitosis do not differ compared to wild–type, perhaps due to compensatory increased cell death. Eml1, like Pax6, plays therefore an important role, limiting RGCs to the VZ during early cortical development.

Human EML1 (O00423.1) shares 57% amino acid identity (397 identical residues over a 686 amino acid region) with sea urchin EMAP (Q26613), found to localize to the mitotic spindle, as

well as to interphase microtubules[24]. In epithelial cells, we observed both cytoplasmic and microtubule localizations of tagged Eml1, which may suggest that it can associate with unpolymerized as well as polymerized tubulin. Indeed, EML1 has recently been shown to associate with both[35]. EMAP family members have been reported to influence dynamics, destabilize or stabilize microtubules[25,43] and several are regulated by phosphorylation during the cell cycle[26,27]. Underlining Eml1's microtubule function, we observed an enrichment of wild–type Eml1 around the microtubule organizing center and regrowing microtubules, and the T243A patient mutation, occurring in the highly conserved HELP domain, altered this localization. These data point to an essential role of Eml1 in association with dynamic microtubules.

In neuronal progenitor cultures, tagged Eml1's localization is cell cycle–dependent, enriched at the equatorial, interzonal region during anaphase and telophase, and at the spindle poles during metaphase. The endogenous protein not analysed here, may exhibit a similar profile. Indeed, endogenous localizations of other members of the EMAP family, were also reported to be cell–cycle dependent[26,27,30]. EML3 co–localizes with midbody microtubules in HeLa cells and is required for correct spindle function[30]. The midbody, a transient equatorial structure important for cell separation[31], is present in the apical ventricular end–foot of RGCs[44,45], and apical–basal attachments may indeed be key to the *HeCo* phenotype. However, the ventricular lining shows no obvious gross discontinuities in *HeCo* brains, unlike some other models[11,46]. Notably though, as well as less mitotic cells in this region in *HeCo*, we also observe spindle orientation defects. The increased number of oblique cleavage orientations is predicted to lead to a higher proportion of daughter cells which do not inherit the apical membrane, and to cell detachment[15]. In some other models abnormal spindle orientations are associated with increased cell cycle exit, premature neurogenesis and microcephaly[47]. In others still, increased horizontal and oblique divisions favour the number of basal progenitors resulting in increased cortical thickness[48]. *HeCo* mice are normocephalic[12] (showing a similar overall number of proliferating RGCs and basal progenitors,

Supplementary Fig. 2), but all patients are megalencephalic, which may suggest abnormal proliferation, perhaps also of OSVZ progenitors, critical during cortical expansion[21]. Indeed, *HeCo* mice may most resemble LGN mutant mice exhibiting changed spindle orientations and re–distributed progenitors, with no apparent effect on cell fate[15]. They have the added particularity of forming heterotopic masses in the IZ in late embryogenesis. These data hence contribute another model to the growing list of spindle orientation mouse mutants which each appear to exhibit variations and specificities in their cortical phenotypes[49]. Spindle dynamics and orientation, midzone function and cell cycle properties are coordinated during brain development[44,45] and loss of microtubule–binding Eml1 hence perturbs these processes, contributing to the generation of ectopic progenitors. Further studies are required to fully comprehend the details of this phenotype.

Our data strongly reinforce the concept that ectopic proliferation in the IZ during corticogenesis can contribute to the pathogenesis of SH in the rodent[9,11,50]. Our study also firmly links the *HeCo* phenotype to giant ribbon–like heterotopia, megalencephaly and polymicrogyria in human, hence highlighting progenitor defects in the pathogenesis of these disorders. We can hence distinguish these malformations associated with mutations in *EML*1 from those due primarily to intrinsic neuronal migration defects, giving rise to classical SBH in human and a preserved neocortex in the mouse[3-6]. Identification of *EML*1, a microtubule–binding protein with a specific role in progenitors, provides a new element to decipher the finely regulated molecular and cellular mechanisms underlying normal cortical development.

Database accession numbers

GEO submission GSE56907 (microarray data), Genbank accession KJ734704 (*HeCo*_Etn sequence), KJ734705 (Exon 22 skipped_*HeCo* transcript sequence), KJ734706 (Exon 21&22 skipped_*HeCo* transcript sequence). MGI submissions (genotyping data).

ACKNOWLEDGEMENTS

We thank the Inserm Avenir program, the French Agence National de la Recherche (ANR– 08–MNP–013, ANR–13–BSV4–0008–01, ANR Blanc 1103–01, projet R11039KK, ANR E–Rare Program, convention 2011–RaARE–012–01), the Fondation Bettencourt Schueller and the Federation pour la recherche sur le cerveau (FRC) for grants awarded to FF or JC, the FRC Rotary for an equipment grant awarded to the IFM, and the Swiss National Science Foundation (SNSF)–SPUM–33CM30–124089 and 33CM30–140332, the Fondation Gianni Biaggi de Blasys and the SNSF–31003A–135574 for grants awarded to AC and SNSF 31003A–125379 to EW. We are particularly grateful to families and clinicians for access to their DNA samples. We also thank B. Barry, C. Walsh and American clinicians for access to certain of their severe heterotopia cases. We thank W. van Ijcken for performing exome sequencing and R. Schot for excellent analysis of exome data of family 3489. We also thank W.B. Dobyns, Seattle Children's Research Institute for critical review and classification of the MRI of family 3489. We are grateful to David Turner and Nathaniel Heintz for reagents. We thank the imaging and animal house platforms at the IFM and the Région Ile–de–France for support, as well as the animal facility and the CIF at the DNF, Switzerland. We thank J. Lemarchand, Y. Saillour, D. Derbala, M. Foglio, A. Boland, D. Zelenika, I. Gut, J.P. Hornung, D. Valloton, M. Niquille, C. Devenoges, N. Narboux–Neme, A. Cabrera, E. Bruel–Jungerman, R. Khalaf–Nazzal, X. Jaglin, T.D.H. Iuliano, M. Karababa, N. Magalhaes, M. Nosten–Bertrand, G. Grannec, A. Houllier, I. Moutkine for their contributions to this work. We are grateful to M. Groszer, J–A Girault, A. Houdusse, C. Moores, R. Bayliss, A. Fry, S. Cappello, M. Götz for interesting discussions. The group of FF is affiliated with the Ecole des Neurosciences de Paris (ENP) and the Bio–Psy laboratory of excellence. The research leading to a part of these results received funding from the European Union Seventh Framework Programme FP7/2007–2013 under

the project DESIRE (grant agreement n°602531), la Fondation pour la Recherche Médicale (FRM, J Chelly – Equipe FRM 2013: DEQ2000326477), la Fondation JED–Belgique.

LEGENDS TO FIGURES

Figure 1 *HeCo* heterotopia and cell accumulation in the dorso–medial regions of developing *HeCo* cortex. (**a**) Nissl stained brain section from a *HeCo* mouse showing bilateral bands of subcortical heterotopic neurons (# right) compared to a wild–type section (left) . (**b,c**) At E17 in the *HeCo* cortex, early–born $Tbr1^+$ (**b**) and late–born $Cux1^+$ (**c**) neurons are trapped within the heterotopia (#). Nestin labeling shows disorganized RGCs processes throughout the heterotopia (**b,** far right). (**d**) At P3, $Tbr1^+$ neurons (top) have reached layer VI whereas many $Cux1^+$ neurons (below) remain trapped within the heterotopia and the radial extent of the *HeCo* $Cux1^+$ cortical layer II/IV is reduced above the heterotopia compared to wild–type. A column of $Cux1^+$ cells is present between the heterotopia and layer II/IV (**d,** lower, arrow). Arrowheads indicate similar regions. Cell nuclei of coronal brain sections were counterstained with Hoechst. Ctx, cortex; Hip, hippocampus; LV, lateral ventricle. Scale bars: 2 mm (**a**), 400 μm (**d,** left and middle), 200 μm (**b,c,d,** right) and 25 μm (**b,** far right). Each of these observations was reproduced at least 3 times.

Figure 2 No changed parameters of migrating cells in *HeCo* and wild–type mice. (**a**) Density and tracking of $EGFP^+$ cells 3 DIV after E15.5 electroporation, are shown for wild–type and *HeCo* slices (migration parameters: 1 section/animal; speed and pause frequency calculated in n=3 wild–type, n=83 cells, n=3015 tracking points, n=5 *HeCo,* n=86 cells, n=3064 tracking points; pause duration measured for n=323 wild–type, n=319 *HeCo* cell pauses*)*. Similar trajectories of wild–type and *HeCo* $EGFP^+$ neurons within the CP were confirmed by calculating the angle of migration (1 section/animal n=3 wild–type, n=5 *HeCo*, measured for n=2536 wild–type, n=2514 *HeCo* cell

movements) and are illustrated by cell tracking trajectory orientations and 3 sequential images (arrow heads). Some stationary *HeCo* $EGFP^+$ cells with horizontal orientation were observed (white arrow). (**b**) After electroporation at E15.5, less $EGFP^+$ cells reached the cortex in P3 *HeCo* embryos, and they fail to form a distinct cortical layer II/IV although the morphology of cells within the CP is similar to wild–type. Many cells remain sequestered in the heterotopia (#).Coronal brain sections; cell nuclei counterstained with Hoechst. (**c**) Representative images of *in vivo* CMFDA–labeled transplanted cells reaching the CP at E17.5 (19 sections, 293 cells from n=10 wild–type, 42 sections, 426 cells from n=18 *HeCo*). Similar cell distribution in the different zones was observed after transplantation of either wild–type or *HeCo* E14.5 dissociated cells. Scale bars, 200 μm (**b,** left), 100 μm (**b,** right, **c**), 90 μm (a–left) 40 μm (a–density), 30 μm (tracking and video images t:0, 60',120'), 25 μm ().

Figure 3 Proliferation defects in *HeCo* cortex**.** (**a**) At E15, $BrdU^+$ progenitors are observed in all *HeCo* zones and inter–mix with $Tbr1^+$ neurons, while WT $BrdU^+$ cells are mostly restricted to the VZ/SVZ. (**b**) At E13, increased numbers of $BrdU^+$ cycling progenitors are present in the *HeCo* forebrain. After a 30 min BrdU pulse (left) ectopic *HeCo* progenitors are observed in the IZ/CP as in (**a**), with an increased labeling index (**c**, 3 sections/animal n=4; each dot is representative of one section, unpaired *t*–test, ALL layers, p=0.016, 13.051 d.f., *t*=–2.774; Multiple Factor ANOVA (MFA) 1 d.f, VZ p=0.075, *F*=3.260, SVZ p=0.194, *F*=1.715, IZ p=6.77 x 10^{-21}, *F*=164.408, CP p=1.49 x 10^{-15}, *F*=99.241). After a 24 h BrdU pulse (**b**, right), cell cycle exit is reduced in the SVZ, IZ and CP (**c**, right, 3 sections/animal n=3; unpaired *t*–test, ALL layers, p=0.009, 15.433 d.f., *t*=2.967; MFA 1 d.f., VZ p=0.074, *F*=3.296, SVZ p=0.007, *F*=7.842, IZ p= 3.86 x 10^{-10}, *F*=54.586, CP p= 7.31 x 10^{-27}, *F*=327.536). The VZ is reduced in thickness in the mutant. (**d**) At E19, *HeCo* ectopic progenitors surround the heterotopia (#) and are often $BrdU^+$ and $Ki–67^+$. (**e**) E13 Caspase 3 immunostaining reveals increased apoptotic cells in *HeCo* (3 sections/ animal n=6; unpaired *t*–test,

p=4.73 x 10^{-16}, 33.847 d.f, *t*=-5.436). Scale bars, 200 μm (lower magnification **a,d**), 100 (**c,e**; higher magnification **a,d**) and 50 μm (**d,** far right). Individual data points showing dispersion and corresponding means are shown in dot plots.

Figure 4 Genetic linkage of the *HeCo* mutation and identification of a retrotransposon in *Eml*1. (**a**) The 12q *HeCo* candidate region identified by first (1) and second (2) rounds of genotyping and the final candidate region (3) between rs29151683 and a non referenced SNP in *Dlk*1. ▼, internal SNPs homozygous for the NOR–*HeCo* alleles in all affected F2 mice; ▽, flanking boundary SNPs and additional informative SNPs from genes *Dlk*1, *Dync1h*1, *Mark*3, and *Adam*6, heterozygous (HZ) in some F2 individuals. Black bars, regions of homozygosity; grey bars, excluded regions; dotted bars, non–excluded regions (informative SNPs and individuals in **Supplementary Table 1**). (**b**) *Eml*1 gene structure (assembly NCBI37/mm9, July 2007). The canonical isoform (NCBI NM_001043335.1) begins in exon 2. (**c**) *Eml1* exon 22 could not be amplified from *HeCo* genomic DNA. (**d**) Aberrant transcripts detected by nested RT–PCR between exons 19 and 23, from two distinct *HeCo* (1 and 2) samples; RT, reverse transcriptase. (**e**) ETn element insertion identified by sequencing a >5 kb intron 22 PCR product. (**f**) Schema of the *Eml1* ETn element with chimeric transcripts detected by RT–PCR. Some *Eml*1 transcripts finish in the ETn, others start in the ETn and finish in *Eml*1 exon 23. Black bars, PCR products; ⇨, *Eml*1 primers; ➞, ETn primers; SD, splice donor, SA, splice acceptor, pA, potential polyadenylation sites; STOP, in–frame stop codons; ATG, potential start codons (the ETn contains additional SD, SA and pA sites, not represented here). Full length gels are presented in **Supplementary Fig. 11**.

Figure 5 *Eml*1 brain expression and *HeCo* and RNAi rescue. (**a–i**) *Eml*1 expression in mouse (**a–g**) and ferret (**h,i**). (**a–c,e**) *Eml*1 is in the VZ at E13.5 (**a,** blue staining) and the VZ and CP at E14.5 (**b**) and E15.5 (**c,e**). At E17.5 a strong CP with no further VZ expression is observed (**d,f**). (**e,f**)

Labeling of the medial edge of the striatum (arrow). In adult (**g**) thalamus and piriform cortex are labeled (arrow). (**h,i**) Ferret *Eml*1 is detected strongly in the CP and in the proliferative layers (**h**, arrows). Observations reproduced 3 times, mouse, and 2 times, ferret. (**j**) Electroporation of BLBP–Eml1–IRES–EGFP in *HeCo* reduces the number of BLBP–EGFP$^+$ progenitors in the SVZ/IZ (n=4 animals/condition, 2 sections/animal, total cells 777 *HeCo*–Ctrl, 851 *HeCo*–rescue). (**k**) *Eml*1 knockdown in WT embryos by *in utero* electroporation of an shRNA construct increases the number of BLBP–EGFP$^+$ progenitors in the SVZ/IZ (arrowheads) and this is rescued by BLBP–Eml1–IRES–GFP (**l**, 9 sections from n=4 Ctrl, n=4 RNAi, n=5 Rescue, total cells 557 Ctrl, 758 RNAi, 771 Rescue, MFA p=0.0001, 2 d.f., F=14.219; unpaired t–test with 1 d.f: Ctrl–RNAi, p=0.0011, t=15.819; RNAi–rescue, p=0.0004, t=19.621; Ctrl–Rescue p=0.8651, t=0.030). (**m**) Ectopic proliferating cells (Ki67$^+$EGFP$^+$) were observed (two experiments). MZ, marginal zone; SP, subplate; IZ, intermediate zone; OSVZ, outer subventricular zone; ISVZ, inner SVZ. **a–g**, coronal, **h,i**, sagittal sections. Scale bars 500μm (**h**), 400 μm (**f,g**), 200 μm (**b–e,i**), 100 μm (**a**,**j,k**), 15 μm (**m**). Individual data points showing dispersion and corresponding means are shown in the dot–plot.

Figure 6 YFP–EML1 in neuronal progenitors *in vitro* and features of *HeCo* progenitors**.** (**a**) YFP–EML1 puncta accumulate during telophase in the region of the midzone and remnants are sometimes observed asymmetrically after cell separation. Far right, enlargements of boxed areas. Observations reproduced more than 5 times. (**b**,**c,**) In E13 *HeCo* brains, P–vim$^+$ RGCs are decreased in VZ while increased in IZ/CP, (**c**, 3 sections/animal, n=6/genotype; MFA 1 d.f., VZ p=5.94 x 10-7, F=27.470, SVZ p=0.246, F=1.356, IZ p=0.009, F=6.975, CP p=0.124, F=2.402; unpaired t–test, ALL layers p=0.964, 33.661 d.f., t=-0.045. Right, P–vim$^+$/Pax6$^+$ sections: 8 WT, 9 *HeCo*, n=3/genotype; MFA 1 d.f., VZ p=0.361, F=0.847, SVZ p=0.003, F=9.885, IZ p=2.57 x 10^{-7}, F= 33.207, CP p=6.94 x 10^{-6}, F=23.975; unpaired t–test, ALL layers p=0.104, 14.426 d.f., t=1.738. Rare P–vim$^+$/Tbr2$^+$ 3 sections/animal, n=3/genotype, MFA, 1 d.f, VZ, p=0.027, F=5.096, SVZ

p=0.184, *F*=1.801, IZ p=1.30 x 10^{-4}, *F*=16.587, CP p= 5.29 x 10^{-6}, *F*=24.701; unpaired *t*–test, ALL layers p=0.550, 15.609 d.f., *t*=0.612). (**d**) Some P–vim^{+} basal processes appear misoriented (**b**, arrows). P–vim^{+}/Pax6^{+} cells are shown by filled arrow heads, P–vim^{+} asymmetrically dividing cells by empty arrow heads. Normal *HeCo* ventricle lining with typical honeycomb β catenin labeling. (**e**) The proportion of anaphasic nuclei with an oblique cleavage plane is significantly increased in *HeCo* at E13 (5 sections/animal, n=8/genotype, total cells 302/genotype; χ^2–test 2 d.f., p=5.09 x 10^{-5}, χ^2=19.770, standardized residual (s.r.) for 0–30°=0.1 p=0.920 (wild-type 6 +/- 4.62 %, *HeCo* 7 +/- 3.38 %, s.r 30–60°=2.9 p=0.004 wild-type 9 +/- 3.34 %, *HeCo* 22 +/- 3.51 %; s.r. 60–90°= –1.3 p=0.194, wild-type 85 +/- 3.22 %, *HeCo* 71 +/- 3.36 %) and at E16 (not shown). Scale bars 100 μm (**b,** low power views), 20 μm (**b** higher power views**, d**), 8 μm (**a**), 5 μm (**e**), and 1 μm (**a** far right). Individual data points showing dispersion and corresponding means are shown in dot–plot.

Figure 7 Mutations in human *EML*1. (**a–c**) *EML*1 mutations in two families with ribbon–like heterotopia. (**a**) Pedigrees of the non–consanguineous family with three affected boys and the consanguineous family with two affected sibs. (**b**) Sequence chromatograms showing the 2 mutations in family P135 (black bars). (**c**) Patient axial T1 weighted MRI sections (middle and lower rows, left and centre) show huge subcortical masses (left, arrowhead) that start at the ventricles (centre) and expand to the subcortical white matter. The cortex close to the lesion is polymicrogyric in P135–5 (left, arrow). White matter is present between the heterotopia and cortex. Corpus callosum agenesis and mild brainstem hypoplasia are obvious when comparing patient (P135–5 and 3489–4, 6 and 4 years old respectively) and control (ctrl, 6 years old) T1 sagittal sections (arrowhead, corpus callosum; arrow, brainstem). Moderate ventricular enlargement, most prominent in the left lateral ventricle, is observed in patient P135–5, and patient 3489–4 suffers from hydrocephaly, plagiocephaly and dolichocephaly. Cerebellum and hippocampus are normal in patient P135–5; the hippocampus is hypoplastic, the basal ganglia are dysplastic and the cerebellum

is enlarged in patient 3488–4. Patient P135–5 and control images are presented at the same scale. (**d**) Region of conserved HELP domain of the EML1 protein containing W225 and T243 residues (O00423, human EML1; Q9HC35, human EML4; O95834, human EML2; Q26613, sea urchin EMAP; O45487, *Caenorhabditis elegans* ELP1; Q9N9X3, *Euplotes octocarinatus* Emapl, XP_002084895, Drosophila EMAP).

Figure 8 Association of recombinant wild–type and mutant Eml1 with microtubules. (**a**) A fraction of wild–type tagged–Eml1 is associated with the microtubule cytoskeleton in Vero cells (far right, higher magnification of boxed area). (**b,c**) GST–EML1 interacts directly with microtubules *in vitro*. (**b**) In the presence of taxol–stabilized microtubules (left), a major fraction of GST–EML1 (MW 116 kDa) cosediments with the microtubule pellet (P). With the same amount of unpolymerized tubulin (right), most GST–EML1 remains in the supernatant (S). (**c**) After incubation with microtubules, the GST control protein (MW 26 kDa) remains in the supernatant. These observations were reproduced more than 5 (**a**) and 3 times (**b**,**c**). (**d-f**) Effect of the T243A mutation. Different staining patterns of cells (transfected wild–type or T243A construct, cold treated and restored for 2 min at 37°C) were assessed (**d,** n=13 randomly chosen cells per condition, raw data from one representative experiment, reproduced 3 times). (**e**) Wild–type Eml1–labeled puncta (left) strongly associate with repolymerizing microtubules while mutant Eml1 (T243A) is less well associated (right) although nascent microtubules are detected with antibody to α–tubulin. The extent of colocalization is indicated in positive PDM (product of the difference from the mean) images, showing intensities above the mean for both fluorescent channels (yellow, strongest colocalization). **(f)** Wild–type EGFP–Eml1 sediments with microtubules (P1 fraction) after one cycle of depolymerisation–repolymerisation. Compared to wild–type protein, reduced amounts of mutant EGFP–Eml1 (T243A) were sedimented (n=3 independent experiments). Scale bars 10 μm (**e**) and 5 μm (**a**). Full length blots are presented in **Supplementary Fig. 11**.

ONLINE METHODS

Animals. Research was conducted according to national and international guidelines (EC directive 86/609, French MESR 00984.01) with protocols followed by local ethical committees. WT and *HeCo* mice on a NOR–CD1 genetic background (outbred stock) were used for developmental analyses. For primary neuronal cultures and *in situ* hybridization, Swiss and NOR–CD1 mice were used. Pigmented ferrets (*Mustela putorius furo*) were used. For staging of embryos, the day of vaginal plug was considered as E0.5. Mice were housed with a standard 12 h light/dark schedule (lights on at 07:00 a.m.).

Immunohistochemistry and confocal microscopy Mouse embryo brains were fixed by immersion overnight at 4°C in 4% w/v paraformaldehyde (PFA) in 0.1M phosphate buffer, pH 7.4. Brains were included in a solution of 75 mg/ml agarose and 150 mg/ml sucrose in Phosphate Saline Buffer (PBS) 1X (Dulbecco's PBS, Gibco Invitrogen) and cut in coronal sections (70 µm) using a vibrating blade microtome (Leica VT1000 S). Postnatal mice were anaesthetized with sodium pentobarbitone and perfused with PFA. Brains were postfixed 2 h, cryoprotected in 30 % w/v sucrose and cut in coronal frozen sections (30–50 µm). Immunodetection was performed using standard protocols. The following primary antibodies were used: mouse monoclonal anti–GFP (G6539 Sigma Aldrich, 1/400), anti–Ki–67 (556003 BD Pharmingen, 1/200), anti–BrdU (MON8003 Monosan, 1/100), anti–β–catenin (C19220 BD Transduction Lab, 1/200), anti–Nestin (Rat–401 DSHB, 1/200), and anti–Phospho–vimentin (AB22651 Abcam, 1/200); rabbit polyclonal anti–GFP (A6455 Invitrogen, 1/700–1/1000), anti–Caspase–3 (9664 Cell Signaling, 1/200), anti–Cux1 (sc13024 Santa Cruz Biotechnology, 1/400), anti–Ki–67 (301103 Novocastra, 1/200), anti–Par3 (07–330 Millipore, 1/200), anti–Pax6 (PRB–278P Covance, 1/500), anti–Tbr1 (AB31940

Abcam, 1/500), anti–Tbr2 (AB23345 Abcam, 1/500), anti–GFAP (Z0334 Dako, 1/400), and anti–S100β (HPA015768 Sigma–Aldrich, 1/2000); goat polyclonal anti–Dcx C–18 (sc–8066 Santa Cruz Biotechnology, 1/300), and anti–Sox2 (MAB2018 R&D Systems, 1/500); rat monoclonal [HTA28] to Histone H3 (phospho S28) (AB10543 Abcam, 1/200). We checked with other researchers in the field who confirmed most other antibodies prior to our use. Fluorescent–stained sections were imaged with confocal microscopes (Zeiss LSM 710 Quasar or Leica SP5) equipped with 10x, 20x, 40x oil Plan–NEOFLUAR, and 63x oil Plan–Apochromat objectives. Fluorophore excitation and scanning were performed with an Argon laser 488 nm (blue excitation for GFP, Alexa 488), with a HeNe1 laser 543 nm (green excitation for Alexa 594) and a Diode laser 405 nm (for Hoechst staining). To obtain the whole Z–stack dataset, we used the mode ‘‘Surpass’’ and single sections of a Z–stack were displayed by using the ‘‘Slice’’ mode of Imaris.

Ex vivo **and** ***in utero*** **electroporation, transplantation and confocal time–lapse microscopy.** Pregnant mice were sacrificed with pentobarbital, E15.5 embryos collected in cold dissecting medium (MEM, Gibco, with 15 mM glucose and 10 mM Tris, pH 7.4). The expression vector pCAGGS–GFP (30 µl at 0.5µg/µl in sterile PBS containing 20% w/v Fast–blue) was injected into the ventricular region of embryonic brains by a pneumatic picopump (Picospritzer III, Parker Hannifin Corporation). Embryos were placed into HBSS 1X medium (Gibco), electrodes (System CUY650P5 NepaGene Co) were maintained around the embryo head with a 45° angle and plasmids electroporated by discharging a 4000 µF capacitor charged to 45 V (5 electric pulses of 50 ms with 500 ms intervals) with a CUY21 electroporator. After electroporation brains were embedded in 3% w/v low–melting point agarose (Invitrogen). For imaging migrating neurons, an *in vitro* model of organotypic slices was used (modified from ref. 51). Coronal sections (250 µm–thick) were cultured for 3 DIV on nucleopore Track–Etch membranes (1 µm pore size; Whatman) in slice culture medium (SCM: BME/HBSS, Invitrogen) supplemented with glutamine, 5% v/v horse serum, and

penicillin/streptomycin. Temperature was maintained at 37ºC (microscope incubator system Life Scientific) and slices were perfused with SCM medium containing a gas mixture of 5% CO2/ 95% O2. $EGFP^+$ neurons were imaged for 10 hrs with a 20X and a 60X immersion lens at 15 min intervals using the fast scan function of the Leica SP5 confocal microscope resonant scanner. Image captures and all peripherals were controlled with Leica software. Pictures were processed and converted into *.AVI movies using Imaris and Metamorph 6.0. Using the tracking function of Metamorph software 6.0, neuron traces were analyzed. Migration parameters (basal rate of migration, frequency and duration of the intervening pauses, absolute angle) of IZ and CP migrating neurons were assessed. Overall fluorescence intensities were measured manually with Imaris software and $EGFP^+$ cells in the CP were counted in WT and *HeCo* cortical sections of 50 µm in a defined volume stack using Imaris manual volume tool.

For *in utero* electroporations, E14.5 and E15.5 timed–pregnant Swiss, *HeCo* and NOR–CD1 mice were anesthetized with isoflurane (3–4 % during induction and 2–2.5 % during surgery) and embryos were exposed within the intact uterine wall after sectioning the abdomen. Embryos were electroporated as above with combinations of the expression vectors pShRNA, pShRNA–control, pBLBP–GFP, pBLBP–Eml1–IRES–GFP and pBLBP–IRES–GFP (2 µl at 1 µg/µl with Fast Green 0.3 mg/ml), and with the expression vector pCAG–GFP (2 µl at 2 µg/µl with Fast Green 0.3 mg/ml), using five electrical square unipolar pulses (amplitude: 45 V; duration: 50 ms; intervals: 950 ms) powered by a Nepa Gene (model CUY21 EDIT Square Wave Electroporator; NEPA GENE) or a BTX (model BTX ECM 830; Harvard Apparatus) electroporation apparatus. The embryos were placed back in the abdominal cavity and the development was allowed to continue until either E15.5 or P3.

For transplantation experiments, cortical cells were dissociated from E14.5 WT and *HeCo* mouse brains, stained with CMFDA Cell Tracker, and injected into E14.5 WT hosts, as described in

ref. 11. Embryos were left to develop *in utero* and brains analyzed 3 days later. The distribution of CMFDA labeled cells was assessed.

BrdU injections and assessment of proliferation. Timed–pregnant females received a single intraperitoneal injection of BrdU (Sigma–Aldrich, 50 μg/g body weight; 8 mg/ml in 0.15 M phosphate buffer, 0.9 % w/v NaCl, pH 7.4) at E13, E15 and E19. Mice were sacrificed 30 min, 1 h, or 24 h later[52] and brains processed for imunohistochemistry. Alternate sections were chosen for BrdU and Ki–67 or BrdU and Tbr1 double–labeling and preincubated with 2 % methanol v/v to improve BrdU detection.

Cell counting and quantification. After immunohistolabeling Z–stacks were acquired for each coronal section in a multitrack mode avoiding crosstalk artifacts of the fluorochromes. All Z–stacks and image processing were performed with Imaris 4.3 software (Bitplane) and ImageJ 1.48 software (NIH). In general, image stacks contained approximately 25–40 confocal planes each, for optimal z–axis. Counting was performed for each layer (VZ, SVZ, IZ, CP). Labeled cells were counted in a region of interest (ROI), a 100 μm wide and 10 μm deep stripe across VZ, SVZ, IZ and CP, in which thickness was defined by the different layers. For shRNA and rescue experiments BLBP–GFP+ cells were counted in a ROI in sections of 70 μm distinguishing cells restricted to or outside of the VZ. Caspase–3^+ cells were counted in cortical sections of 50 μm, in a defined volume stack using Imaris manual volume tool. For spindle orientations, cortical sections were analysed with Imaris Bitplane® software to determine and count anaphasic shaped nuclei lining the apical membrane (labeled with PAR3) in the VZ. Anaphase nuclei angles were measured with Image J free software "angle tool".

Mouse crosses for genetics screen. For genotyping studies, *HeCo* mice on the NOR–CD–1 background were crossed to C57BL/6J mice, giving rise to an unaffected heterozygote F1 population. Brother–sister matings generated an F2 population with 25 % affected homozygous individuals. Brain sections of each F2 mouse (n= 240, male or female) were analyzed in order to identify mutants.

Whole genome and second round chromosome 12 SNP analyses. DNA samples were prepared from mouse tail biopsies according to recommendations of genotyping platforms. SNP markers were selected based on naturally occurring polymorphisms between C57BL/6 and Sv129 strains, the latter showing the strongest similarity to the NOR–CD–1 background. An array of 1536 SNPs was created and screened using Golden Gate Illumina technology (Illumina, Gmbh). New SNP markers between rs13481624 and rs3692361 on mouse chromosome 12 were screened in the same way.

Differential gene analysis. Total RNA samples were extracted from single hemispheres dissected from NOR–CD1 *HeCo* and WT E18 embryos. E18 RNAs showed a mean RNA integrity number of 9.81 ± 0.12 and a coefficient of variation of 1.26 %. Labeled cRNAs were hybridized to MouseWG–6 v2 expression BeadChips (Illumina, Gmbh). Differential analysis *per* gene was performed with Student *t*–tests. In microarray analyses, quality controls (reference samples, principal component analyses before and after normalization) showed neither batch nor beadchip effect. Bead–averaged data was normalized using quantile normalization (BeadStudio software, Illumina, Gmbh). Real time qPCRs were performed using the SYBRgreen method on total, RQ1 DNAse treated RNA samples, following MIQE guidelines[53]. Values were normalized to the geometric mean of 3 normalization factors found to be the most stable through all samples using the geNorm approach[54]. First strand cDNA was synthesized using 50 ng/µl of total RNA, oligo(dT) and

the Superscript III Reverse Transcriptase kit (Invitrogen). Gene–specific primers were designed using Primer Express Software (PE Applied Biosystems). The 3 genes used for normalization were histone deacetylase 3, Hdac3; Endoplasmic reticulum protein 29, Erp29; ATP synthase, H+ transporting, mitochondrial F0 complex, subunit c (subunit 9), isoform 3, Atp5g3. Amplicon sizes were between 54 and 79 bp. Standard curves were generated from assays made with serial dilutions of cDNA to calculate PCR efficiencies (90 % < efficiency < 105%, with r^2 >=0.998). Threshold cycles (Ct) were transformed into quantity values using the formula $(1+\text{Efficiency})^{-Ct}$. Only means of triplicate with a coefficient of variation of less than 10 % were analyzed. Inter–plate variation was below 8 %.

PCR amplification. Genomic DNA amplifications were performed for each exon and flanking sequences of mouse *Eml*1 from *HeCo* and NOR–CD1 WT samples using standard PCR (primers in **Supplementary Table 4**). Intron 22 was amplified using Pfu turbo DNA polymerase (Agilent Technologies). RT–PCRs were performed from random–hexamer primed cDNAs using standard protocols. PCR products were checked by agarose gel electrophoresis and sequenced using standard Sanger sequencing (Beckmann Coulter Genomics).

Patients and analysis of human *EML*1. Following standard protocols, patient DNAs or blood samples, and informed consent (from all patients' parents) were obtained according to the guidelines of local institutional review boards (IRBs APHP–Délégation Interrégionale à la Recherche Clinique, Paris and Erasmus Medical Center, Rotterdam). Sporadic or familial cases were selected with clinical and brain imaging features compatible with a diagnosis of either lissencephaly or heterotopia. Prior to *EML*1 analysis, patients were found negative for mutations in *DCX* (RefSeq NM_181807), *PAFAH1B1* (RefSeq NM_000430), *ARX* (RefSeq NM_139058), *TUBA1A* (RefSeq NM_006009) or *TUBB2B*. The family with compound heterozygote mutations

was also negative for filamin A mutations. Genomic DNA amplifications were performed for *EML*1 using standard procedures (primers in **Supplementary Table 2**) and PCR products were analyzed by direct sequencing using an ABI3700 DNA analyzer (Applied Biosystems, Foster City, CA). As well as mutations, additional heterozygote amino acid changes were observed in other patients (c.2315 A>G, p.H749R, exon 22; c.292 G>A, p.V75M, exon 2) or present in intronic regions (intron 7, 130 bp after exon 7; intron 21, 10 bp before exon 22).

The mutation for the second consanguineous family (Moroccan) was independently identified by homozygosity mapping and exome sequencing during ongoing studies to identify genetic causes of cortical malformations in a large Dutch cohort (GMM and RO). Parents are healthy. Whole exome sequencing using Agilent Sure Select V4 capturing followed by deep sequencing using Illumina HiSeq was performed (protocol number for genome analysis MEC–2012–387). After filtering for common variants and selecting changes in coding areas and intron/exon boundaries with a predicted effect on the protein, the only homozygote mutation in the areas of homozygosity detected in both affected sibs in SNP array analyses, was found in EML1 on chromosome 14 (p.W225R). This mutation was confirmed by Sanger sequencing in both affected sibs and cosegregation by parental analysis.

P135–3 (French family) was referred for severe developmental delay with congenital macrocephaly. He acquired ambulation with mild spasticity at 4 years, and developed refractory epilepsy with a combination of atypical absences, atonic falls and tonic seizures. At 16 years, he was severely delayed intellectually with severe behavioral and sleep disturbances. P135–4, referred at 8 years for severe intellectual disability and epilepsy had clinical features similar to his brother, generalized epilepsy started at 8 years. P135–5, admitted for severe hypotonia, developed neurological symptoms from the neonatal period. He walked independently at 3 years, but developed behavioral and sleep disturbances. No seizures have yet been reported (8 years). The affected child from the Moroccan (3489) family exhibited macrocephaly and congenital

hydrocephalus, with severe psychomotor delay and seizures. One child is unaffected and the third pregnancy was terminated in the 23rd week because of hydrocephalus shown by ultrasound.

Plasmids and shRNA. Full length mouse *Eml*1 (canonical sequence RefSeq NM_001043335; IMAGE clone 6400458, MGC 62485) was cloned into the pCAGIG vector (Addgene), or the p3X FLAG vector (Sigma–Aldrich) or pEGFP–C3 vector (Clontech) with the tag N–terminal to *Eml*1. Site directed mutagenesis was performed using a Quik Change kit (Stratagene). The pcDNA3.1–YFP–*EML*1 construct was a kind gift from A.M. Fry (University of Leicester, UK). The *Eml*1 shRNA directed against the following 3'–UTR sequence: 5'–GAACTCTGTAGCACTGGTTGT–3', was checked for specificity in sequence databases and cloned in the mU6Pro vector, obtained from the D.L. Turner lab (Michigan, US). Real time qPCRs (Agilent Technologies) were performed from transfected Neuro–2a (N2a) cells using the SYBRgreen method on total, RQ1 DNAse treated, RNA samples, using Eml_RT17–18F and Eml_RT20R primers (see **Supplementary Table 2**). First strand cDNA was synthesized using oligo(dT) primers and the Superscript II Reverse Transcriptase kit (Invitrogen). The Cyclophilin gene was used for normalization. The BLBP–IRES–GFP construct was obtained from the N. Heintz lab (New York, US).

Cell cultures, transfections and immunodetection. COS7 and Vero cells (ATCC) were transfected using Nanofectin (*PAA* Laboratories GmbH) and fixed after 24 h with either 4 % w/v PFA (5 min, 37°C) or ice cold methanol (6 min, –20 °C), or subjected to a detergent extraction in PHEM buffer (60 mM PIPES, 25 mM HEPES, 10 mM EGTA, and 2 mM MgCl2, pH 6.9) + 0.5 % v/v Triton X–100 for 1 min prior to fixation with cold methanol. N2a cells (ATCC) were transfected using the Neon system. For repolymerisation experiments cells were incubated on ice for 30 min 24 h post–transfection, thereafter restored to 37˚C for various intervals before detergent extraction and fixation. Primary cultures from E12.5 cortices were maintained in a B27/N2

medium[55] which is a mixture (1:4) of Neurobasal/B27 medium without vitamin A and DDM medium (DMEM/F12 with GlutaMAX, supplemented with N2, 0.1 mM non–essential amino–acids, 1 mM sodium pyruvate, 500 µg/ml BSA, 0.1 mM 2–mercaptoethanol and penicillin/streptomycin 100 U/ml). Electroporation was performed using an Amaxa mouse Nucleofector kit (Lonza). Cells were fixed in PFA or cold methanol 24 h after electroporation. Immunocytochemistry was performed according to standard procedures and results observed and photographed using either epifluorescence (Leica DM6000) or confocal microscopy (Olympus FV10i). PDM images were generated using Image J. The following primary antibodies were used: mouse monoclonal anti–α–tubulin (DM1A Sigma–Aldrich, 1/10000), anti–GFP, anti–γ–tubulin (GTU–88 Sigma–Aldrich, 1/800), anti–γ–adaptin (A36120 BD Transduction Laboratories, 1/200), anti–KIF1A (612094 BD Transduction Laboratories, 1/75), anti–tyrosinated tubulin (TUB–1A2 Sigma–Aldrich, 1/10000), anti–dynein (IC) (D5167 Sigma–Aldrich, 1/50), anti–spastin (Sp 3G11/1 Santa Cruz Biotechnology, 1/50), and anti–acetylated tubulin (6–11B–1 Sigma–Aldrich, 1/10000); rabbit polyclonal anti–FLAG (F7425 Sigma–Aldrich, 1/500), anti–EML1 (39421 GeneTex 1/300), anti–GFP, anti–Ki–67, anti–Pax6, anti–Tbr2, goat polyclonal anti–Dcx, and rat monoclonal anti–neuronal class III β–tubulin (TUJ1 Covance, 1/1200).

Microtubule sedimentation experiments. Microtubules were polymerized from 10 µg of purified porcine brain tubulin (Cytoskeleton Inc.) in the presence of taxol and and incubated 20 min at 37°C with 1 µg of precleared GST–EML1 or control GST proteins (ProteoGenix). Soluble tubulin (10 µg) was incubated with GST–EML1 under the same conditions. Microtubules were separated from soluble proteins by ultracentrifugation through a 60% v/v glycerol cushion (10 min at 30,000 g using an Airfuge, Beckman). Samples were analyzed by SDS–PAGE and Western blotting using antibodies to GST (G7781 Sigma–Aldrich) and α–tubulin. Transfected N2a cells were lysed by sonication in MEM buffer with 1 mM GTP. After cold–induced microtubule depolymerization and

ultracentrifugation, generating a tubulin–rich supernatant S0, microtubule repolymerization was performed in the presence of 20 μM taxol (Sigma–Aldrich). Microtubules were separated from soluble proteins through a 60% glycerol cushion. After Western blotting using antibodies to α–tubulin and GFP, the ratio of Eml1 to tubulin in the pellet P1 (normalized to the Eml1/tubulin ratio in S0) was determined using ImageJ.

***In situ* hybridization.** Mouse digoxigenin–labeled riboprobes were generated by *in vitro* transcription of a fragment amplified from the *Eml*1 3'UTR region (chr12 nt 109,776,616 to 109,777,469, Genome Browser, http://genome.ucsc.edu/) subcloned in pBluescript II KS vector. To generate the ferret *Eml*1 probe, cDNA was reverse–transcribed from P0 ferret brain total RNA and a fragment amplified using fEml1F, CTTTTCTATGAACTCTTC, and fEml1R, AAGGATACATACAAACAG primers was ligated into pGEM–T–Easy vector (Promega). *In situ* hybridization on ferret brain sections was performed as described previously[22].

Statistical analysis. All data are shown as mean ± s.e.m. Statistical analysis was performed using the IBM SPSS Statistics version 19 (SPSS Inc.) or StatView. The variance was estimated for each set of data and the t–test for partial comparison adapted accordingly. All tests were two–sided. Comparisons of means in 2 groups were made using the unpaired Student *t*–test. For BLBP–GFP electroporations and cell count quantifications, data were subjected to factorial analysis of variance (ANOVA) with conditions, layers, and strains as between factor. Significant main effects were analysed further by *post–hoc* comparisons of means using Student Newman–Keuls *t*–test. The $\chi 2$ test was used for frequency comparisons. Normality was tested using StatView. Data were collected and processed randomly, no data points were excluded. For transplantation, caspase–3 and spindle orientation experiments the data were processed in blind manner. For the other experiments data collection and analysis were not performed blind as the different conditions were clearly

recognizable by the experimenter. No statistical methods were used to pre–determine sample sizes but our sample sizes are similar to those generally employed in the field.

A supplementary methods checklist is available.

AUTHOR CONTRIBUTIONS

MK and FPDT carried out *HeCo* phenotyping and genotyping projects. FPDT characterized Eml1 at the genomic, cDNA and protein levels. FPDT and SB performed Vero, N2A, progenitor and neuronal cultures and analysis of EML1/Eml1 (WT and mutant) in vitro, and mouse in situ hybridization studies, aided by KB. SB performed rescue and RNAi *in utero* electroporations and analyses with help from RB. CL performed time–lapse imaging aided by MK. C de J and VB performed ferret *in situ* hybridizations and *in utero* transplantation analyses. KP, ReO, GMM, NBB, AGleM, PB and JC screened and characterized human patients. KP and NBB followed and screened a human patient DNA panel and controls. ReO and GMM performed exome sequencing and mutation confirmation. RO and J–FD performed transcriptome experiments, genotyping data analysis and submission. DB aided with microtubule experiments. WC performed the second-round mouse genotyping experiment. EW, AC and FF directed the study, analyzed the data and wrote the manuscript greatly helped by MK, FPDT nd SB.

REFERENCES

1. Harding, B. Gray matter heterotopia. In *Dysplasias of cerebral cortex and epilepsy, R. Guerrini, F. Andermann, R. Canapicchi, J. Roger, B.G. Zifkin, P. Pfanner, ed. (Lippincott-Raven, Philadelphia, USA),* 81–*88, (1996).*

2. Jaglin, X.H. & Chelly, J. Tubulin–related cortical dysgeneses: microtubule dysfunction underlying neuronal migration defects. *Trends Genet.* **25**, 555–566 (2009).

3. Hirotsune, S. *et al.* Graded reduction of Pafah1b1 (Lis1) activity results in neuronal migration defects and early embryonic lethality. *Nat. Genet.* **19**, 333–339 (1998).

4. Corbo, J.C. *et al.* Doublecortin is required in mice for lamination of the hippocampus but not the neocortex. *J. Neurosci*. **22**, 7548–7557 (2002).

5. Kappeler, C., *et al.* Magnetic resonance imaging and histological studies of corpus callosal and hippocampal abnormalities linked to doublecortin deficiency. *J. Comp. Neurol.* **500**, 239–254 (2007).

6. Keays, D.A. *et al.* Mutations in alpha–tubulin cause abnormal neuronal migration in mice and lissencephaly in humans. *Cell* **128**, 45–57 (2007).

7. Bai, J. *et al.* RNAi reveals doublecortin is required for radial migration in rat neocortex. *Nat. Neurosci.* **6**, 1277–1283 (2003).

8. Lee, K.S. *et al.* A genetic animal model of human neocortical heterotopia associated with seizures. *J. Neurosci.* **17**, 6236–6242 (1997).

9. Munji, R.N., Choe, Y., Li, G., Siegenthaler, J.A. & Pleasure, S.J. Wnt signaling regulates neuronal differentiation of cortical intermediate progenitors. *J. Neurosci.* **31**, 1676–1687 (2011).

10. Bilasy, S.E. *et al.* Dorsal telencephalon–specific RA–GEF–1 knockout mice develop heterotopic cortical mass and commissural fiber defect. *Eur. J. Neurosci.* **29**, 1994–2008 (2009).

11. Cappello, S. *et al.* A radial glia–specific role of RhoA in double cortex formation. *Neuron* **73**, 911–924 (2012).

12. Croquelois, A. *et al.* Characterization of the HeCo mutant mouse: a new model of subcortical band heterotopia associated with seizures and behavioral deficits. *Cereb. Cortex* **19**, 563–575 (2009).

13. Rosen, G.D. *et al.* Bilateral Subcortical Heterotopia with Partial Callosal Agenesis in a Mouse Mutant. *Cereb. Cortex* (2012 March 27) [Epub ahead of print].

14. Barkovich, A.J. *et al*. A developmental and genetic classification for malformations of cortical development: update 2012. *Brain* **135**, 1348–1369 (2012).

15. Konno, D. *et al.* Neuroepithelial progenitors undergo LGN–dependent planar divisions to maintain self–renewability during mammalian neurogenesis. *Nat. Cell Biol.* **10**, 93–101 (2008).

16. Chenn, A. & Walsh, C.A. Regulation of cerebral cortical size by control of cell cycle exit in neural precursors. S*cience* **297**, 365–369 (2002).

17. Baust, C. *et al.* Structure and expression of mobile ETnII retroelements and their coding–competent MusD relatives in the mouse. *J. Virol.* **77**, 11448–11548 (2003).

18. Welker, E. *et al.* (1996). Altered sensory processing in the somatosensory cortex of the mouse mutant barrelless. *Science* **271**, 1864–1867.

19. Abdel–Majid, R.M. *et al.* (1998). Loss of adenylyl cyclase I activity disrupts patterning of mouse somatosensory cortex. *Nat. Genet.* **19**, 289–291.

20. Hansen, D.V., Lui, J.H., Parker, P.R. & Kriegstein, A.R. Neurogenic radial glia in the outer subventricular zone of human neocortex. *Nature* **464**, 554–561 (2010).

21. Fietz, S.A. *et al.* OSVZ progenitors of human and ferret neocortex are epithelial–like and expand by integrin signaling. *Nat. Neurosci.* **13**, 690–699 (2010).

22. Reillo, I., de Juan Romero, C., García–Cabezas, M.A. & Borrell, V. A Role for Intermediate Radial Glia in the Tangential Expansion of the Mammalian Cerebral Cortex. *Cereb. Cortex* **21**, 1674–1694 (2011).

23. Kelava, I. *et al.* Abundant occurrence of basal radial glia in the subventricular zone of embryonic neocortex of a lissencephalic primate, the common marmoset *Callithrix jacchus*. *Cereb. Cortex* **22**, 469–481 (2012).

24. Suprenant, K.A., Dean, K., McKee, J. & Hake, S. EMAP, an echinoderm microtubule–associated protein found in microtubule–ribosome complexes. *J. Cell Sci.* **104**, 445–450 (1993).

25. Eichenmüller, B., Everley, P., Palange, J., Lepley, D. & Suprenant, K.A. The human EMAP–like protein–70 (ELP70) is a microtubule destabilizer that localizes to the mitotic apparatus. *J. Biol. Chem.* **277**, 1301–1309 (2002).

26. Brisch, E., Daggett, M.A. & Suprenant, K.A. Cell cycle–dependent phosphorylation of the 77 kDa echinoderm microtubule–associated protein (EMAP) in vivo and association with the p34cdc2 kinase. *J. Cell Sci.* **109**, 2885–2893 (1996).

27. Pollmann, M. *et al.* Human EML4, a novel member of the EMAP family, is essential for microtubule formation. *Exp. Cell Res.* **312**, 3241–3251 (2006).

28. Hueston, J.L. *et al.* The C. elegans EMAP–like protein, ELP–1 is required for touch sensation and associates with microtubules and adhesion complexes. *BMC Dev. Biol.* **8**, 110 (2008).

29. Bechstedt, S. *et al.* A doublecortin containing microtubule–associated protein is implicated in mechanotransduction in Drosophila sensory cilia. *Nat. Commun.* **1**:11. doi: 10.1038/ncomms1007 (2010).

30. Tegha–Dunghu, J. *et al.* EML3 is a nuclear microtubule–binding protein required for the correct alignment of chromosomes in metaphase. *J. Cell Sci.* **121**, 1718–1726 (2008).

31. Gromley, A. *et al.* Centriolin anchoring of exocyst and SNARE complexes at the midbody is required for secretory–vesicle–mediated abscission. *Cell* **123**, 75–87 (2005).

32. Hagemeijer, A. & Graux, C. ABL1 rearrangements in T–cell acute lymphoblastic leukemia. *Genes Chromosomes Cancer* **49**, 299–308 (2010).

33. Van Karnebeek, C.D. *et al.* (2002). Further delineation of the chromosome 14q terminal deletion syndrome. *Am. J. Med. Genet.* **110**, 65–72 (2006).

34. Ravnan, J.B. *et al.* Subtelomere FISH analysis of 11688 cases: an evaluation of the frequency and pattern of subtelomere rearrangements in individuals with developmental disabilities. *J. Med. Genet.* **43**, 478–489 (2006).

35. Davies, M.W. *et al*. Crystal structure of EML1 reveals the basis for Hsp90 dependence of oncogenic EML4–ALK by disruption of an atypical β–propeller domain. *Proc Natl. Acad. Sci. USA* **111**, 5195–5200 (2014).

36. Sarkisian, M.R. *et al*. Trouble making the first move: interpreting arrested neuronal migration in the cerebral cortex. *Trends Neurosci*. **31**, 54–61 (2008).

37. Cappello, S. *et al*. Mutations in genes encoding the cadherin receptor–ligand pair DCHS1 and FAT4 disrupt cerebral cortical development. *Nat Genet.* **45**, 1300–8 (2013).

38. Takahashi, T., Goto, T., Miyama, S., Nowakowski, R.S. & Caviness, V.S. Jr. Sequence of neuron origin and neocortical laminar fate: relation to cell cycle of origin in the developing murine cerebral wall. *J. Neurosci.* **19**, 10357–10371 (1999).

39. Stoykova, A., Treichel, D., Hallonet, M. & Gruss, P. Pax6 modulates the dorsoventral patterning of the mammalian telencephalon. *J. Neurosci.* **20**, 8042–8050 (2000).

40. Götz, M., Stoykova, A. & Gruss, P. Pax6 controls radial glia differentiation in the cerebral cortex. *Neuron* **21**, 1031–1044 (1998).

41. Wang, X., Tsai, J.W., Lamonica, B. & Kriegstein, A.R. A new subtype of progenitor cell in the mouse embryonic neocortex. *Nat. Neurosci.* **14**, 555–561 (2011).

42. Shitamukai, A., Konno, D. & Matsuzaki, F. Oblique radial glial divisions in the developing mouse neocortex induce self–renewing progenitors outside the germinal zone that resemble primate outer subventricular zone progenitors. *J. Neurosci.* **31**, 3683–3695 (2011).

43. Houtman, S.H., Rutteman, M., De Zeeuw, C.I. & French, P.J. Echinoderm microtubule–associated protein like protein 4, a member of the echinoderm microtubule–associated protein family, stabilizes microtubules. *Neuroscience* **144**, 1373–1382 (2007).

44. Kosodo, Y. *et al.* Asymmetric distribution of the apical plasma membrane during neurogenic divisions of mammalian neuroepithelial cells. *EMBO J.* **23**, 2314–2324 (2004).

45. Dubreuil**,** V**.**, Marzesco**,** A**.**M**.**, Corbeil**,** D**.**, Huttner**,** W**.**B**.** & Wilsch–Bräuninger**,** M. Midbody and primary cilium of neural progenitors release extracellular membrane particles enriched in the stem cell marker prominin–1. *J. Cell Biol.* **176**, 483–495 (2007).

46. Weimer, J.M., Yokota, Y., Stanco, A., Stumpo, D.J., Blackshear, P.J. & Anton ES. MARCKS modulates radial progenitor placement, proliferation and organization in the developing cerebral cortex. *Development*. **136**, 2965–75 (2009).

47. Feng, Y. & Walsh, C.A. Mitotic spindle regulation by Nde1 controls cerebral cortical size. *Neuron*. **44**, 279–93 (2004).

48. Postiglione, M.P., Jüschke, C., Xie, Y., Haas, G.A., Charalambous, C. & Knoblich, J.A. Mouse inscuteable induces apical–basal spindle orientation to facilitate intermediate progenitor generation in the developing neocortex. *Neuron*. **72**, 269–84 (2011).

49. Lancaster, M.A. & Knoblich, J.A. Spindle orientation in mammalian cerebral cortical development. *Curr. Opin. Neurobiol.* **22**, 737–46 (2012).

50. Fitzgerald, M.P., Covio, M. & Lee, K.S. Disturbances in the positioning, proliferation and apoptosis of neural progenitors contribute to subcortical band heterotopia formation. *Neuroscience* **176**, 455–471 (2011).

51. Niquille, M. *et al.* (2009). Transient neuronal populations are required to guide callosal axons: a role for semaphorin 3C. *PLoS Biol.* **7**(10):e1000230.

52. Martynoga, B., Morrison, H., Price, D.J. & Mason, J.O. Foxg1 is required for specification of ventral telencephalon and region–specific regulation of dorsal telencephalic precursor proliferation and apoptosis. *Dev. Biol.* **283**, 113–127 (2005).

53. Bustin, S.A. *et al.* The MIQE guidelines: minimum information for publication of quantitative real–time PCR experiments. *Clin. Chem.* **55**, 611–622 (2009).

54. Vandesompele, J. *et al.* Accurate normalization of real–time quantitative RT–PCR data by geometric averaging of multiple internal control genes. *Genome Biol.* **3**, research0034.1–research0034.11 (2002).

55. Gaspard, N. *et al.* (2009). Generation of cortical neurons from mouse embryonic stem cells. *Nat. Protoc.* **4**, 1454–1463.

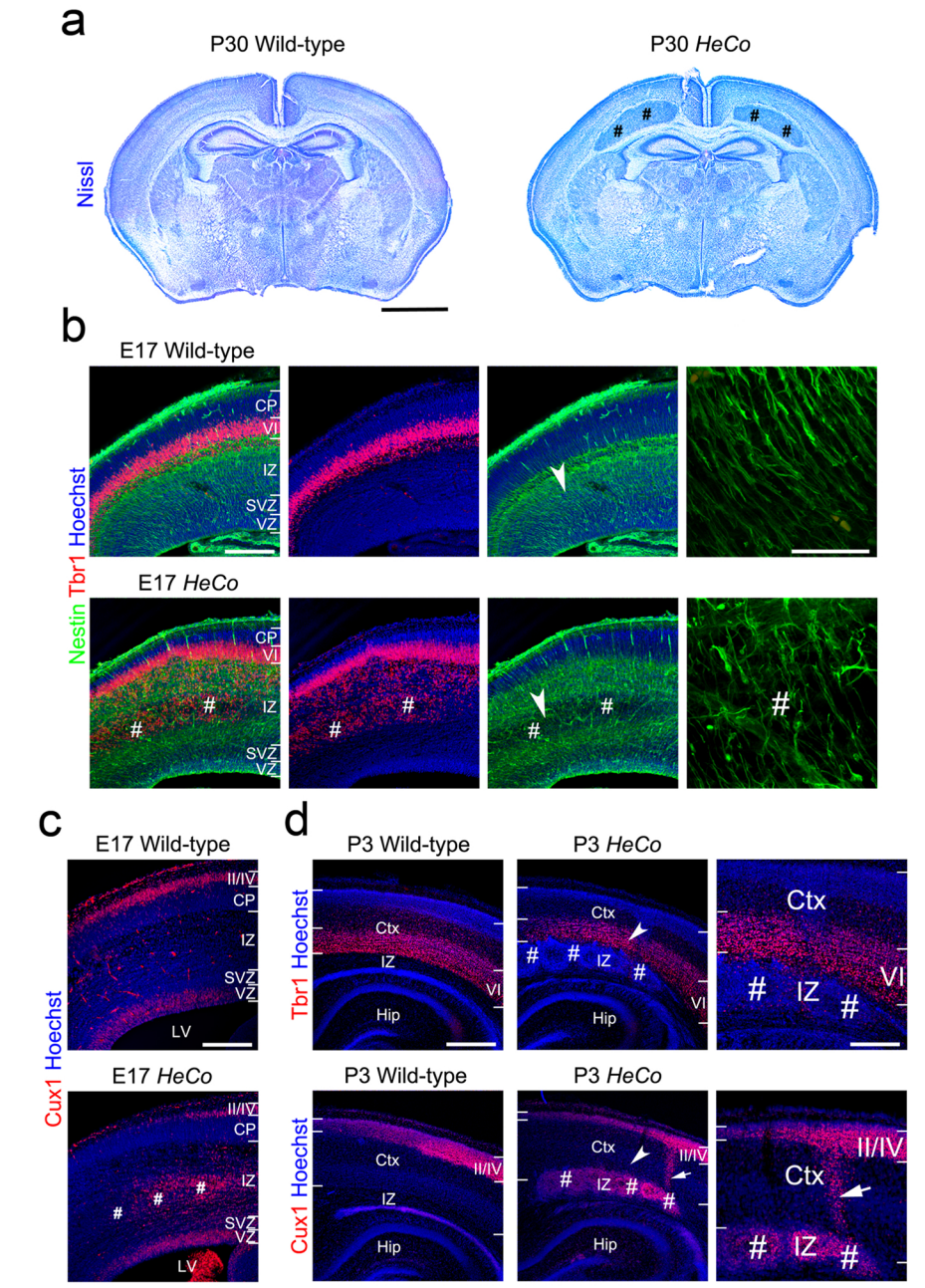
a
P30 Wild-type
P30 HeCo
Nissl
b
E17 Wild-type
CP
VI
IZ
SVZ
VZ
Hoechst
Tbr1
Nestin
E17 HeCo
c
E17 Wild-type
II/IV
CP
IZ
SVZ
VZ
LV
Cux1
Hoechst
E17 HeCo
d
P3 Wild-type
P3 HeCo
Ctx
IZ
VI
Hip
Tbr1
Hoechst
Cux1
II/IV

Figure 1

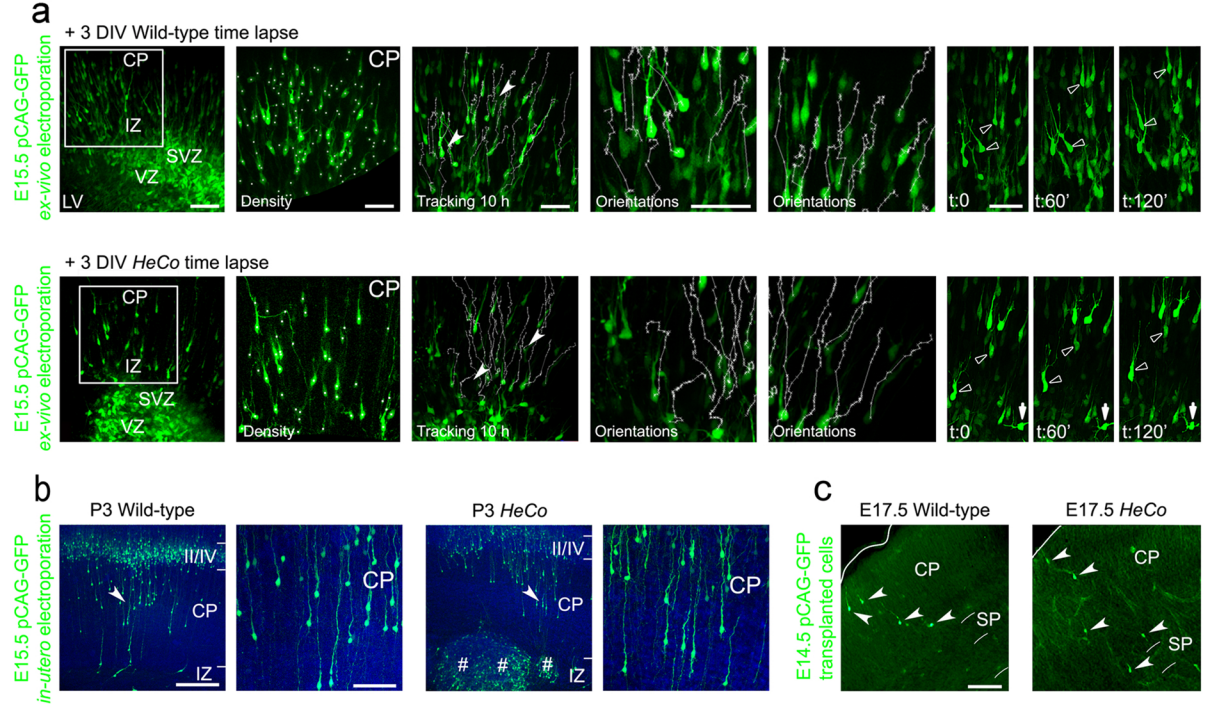
a
+ 3 DIV Wild-type time lapse
E15.5 pCAG-GFP
ex-vivo electroporation
CP
IZ
SVZ
VZ
LV
Density
Tracking 10 h
Orientations
Orientations
t:0
t:60'
t:120'
+ 3 DIV HeCo time lapse
b
P3 Wild-type
P3 HeCo
E15.5 pCAG-GFP
in-utero electroporation
II/IV
#
c
E17.5 Wild-type
E17.5 HeCo
E14.5 pCAG-GFP
transplanted cells
SP

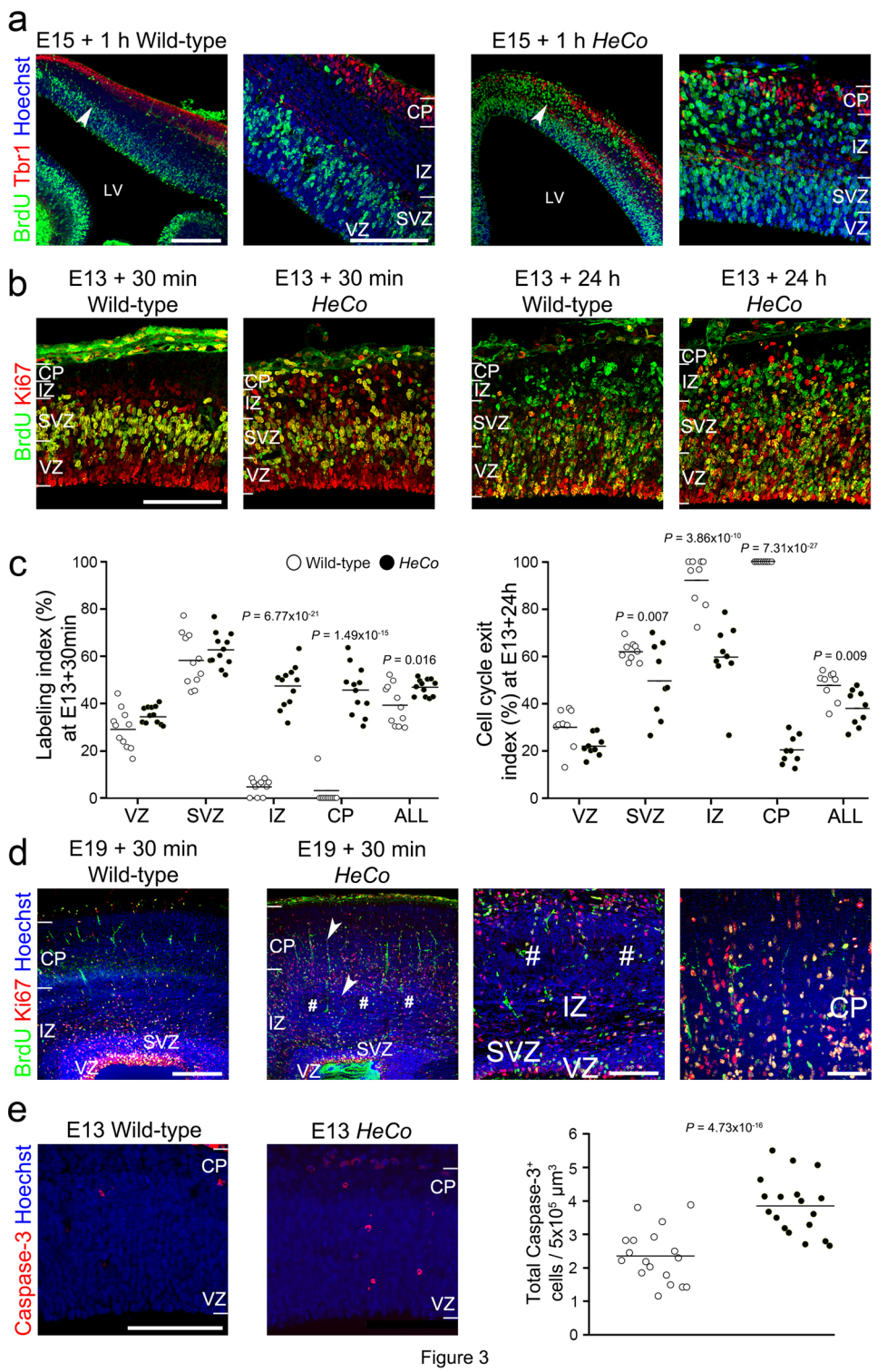
a
E15 + 1 h Wild-type
E15 + 1 h HeCo
BrdU Tbr1 Hoechst
LV
CP
IZ
SVZ
VZ
b
E13 + 30 min Wild-type
E13 + 30 min HeCo
E13 + 24 h Wild-type
E13 + 24 h HeCo
BrdU Ki67
c
Wild-type
HeCo
Labeling index (%) at E13+30min
P = 6.77x10-21
P = 1.49x10-15
P = 0.016
Cell cycle exit index (%) at E13+24h
P = 3.86x10-10
P = 7.31x10-27
P = 0.007
P = 0.009
VZ
SVZ
IZ
CP
ALL
d
E19 + 30 min Wild-type
E19 + 30 min HeCo
BrdU Ki67 Hoechst
e
E13 Wild-type
E13 HeCo
Caspase-3 Hoechst
Total Caspase-3+ cells / 5x10^5 µm^3
P = 4.73x10-16

Figure 3

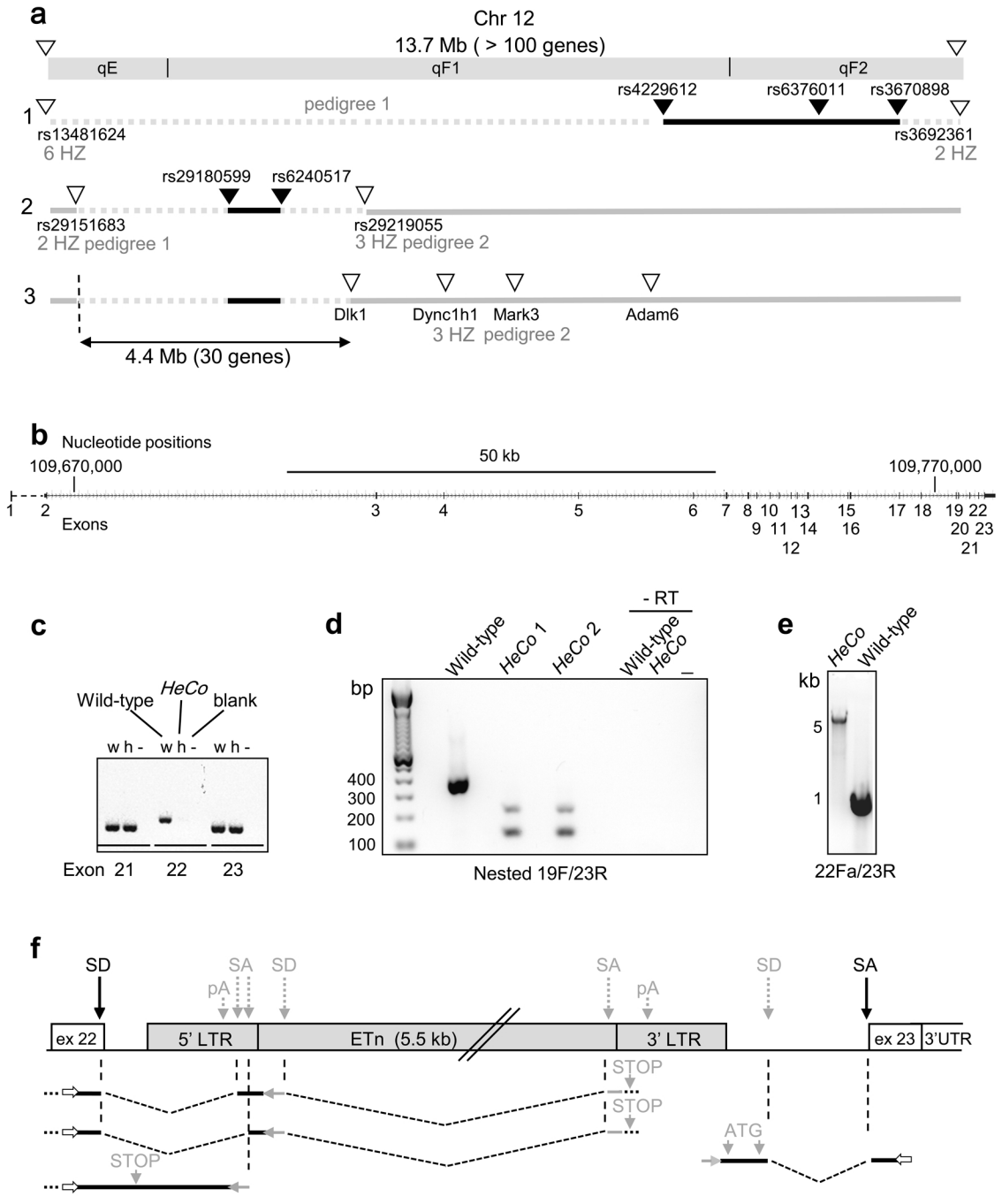
a
Chr 12
13.7 Mb (> 100 genes)
qE
qF1
qF2
1
pedigree 1
rs4229612
rs6376011
rs3670898
rs13481624
6 HZ
rs3692361
2 HZ
2
rs29180599
rs6240517
rs29151683
2 HZ pedigree 1
rs29219055
3 HZ pedigree 2
3
Dlk1
Dync1h1
Mark3
Adam6
3 HZ pedigree 2
4.4 Mb (30 genes)
b
Nucleotide positions
109,670,000
50 kb
109,770,000
Exons
c
Wild-type
HeCo
blank
w h -
Exon 21
22
23
d
- RT
Wild-type
HeCo 1
HeCo 2
bp
400
300
200
100
Nested 19F/23R
e
HeCo
Wild-type
kb
5
1
22Fa/23R
f
SD
SA
pA
ex 22
5' LTR
ETn (5.5 kb)
3' LTR
ex 23
3'UTR
STOP
ATG

Figure 4

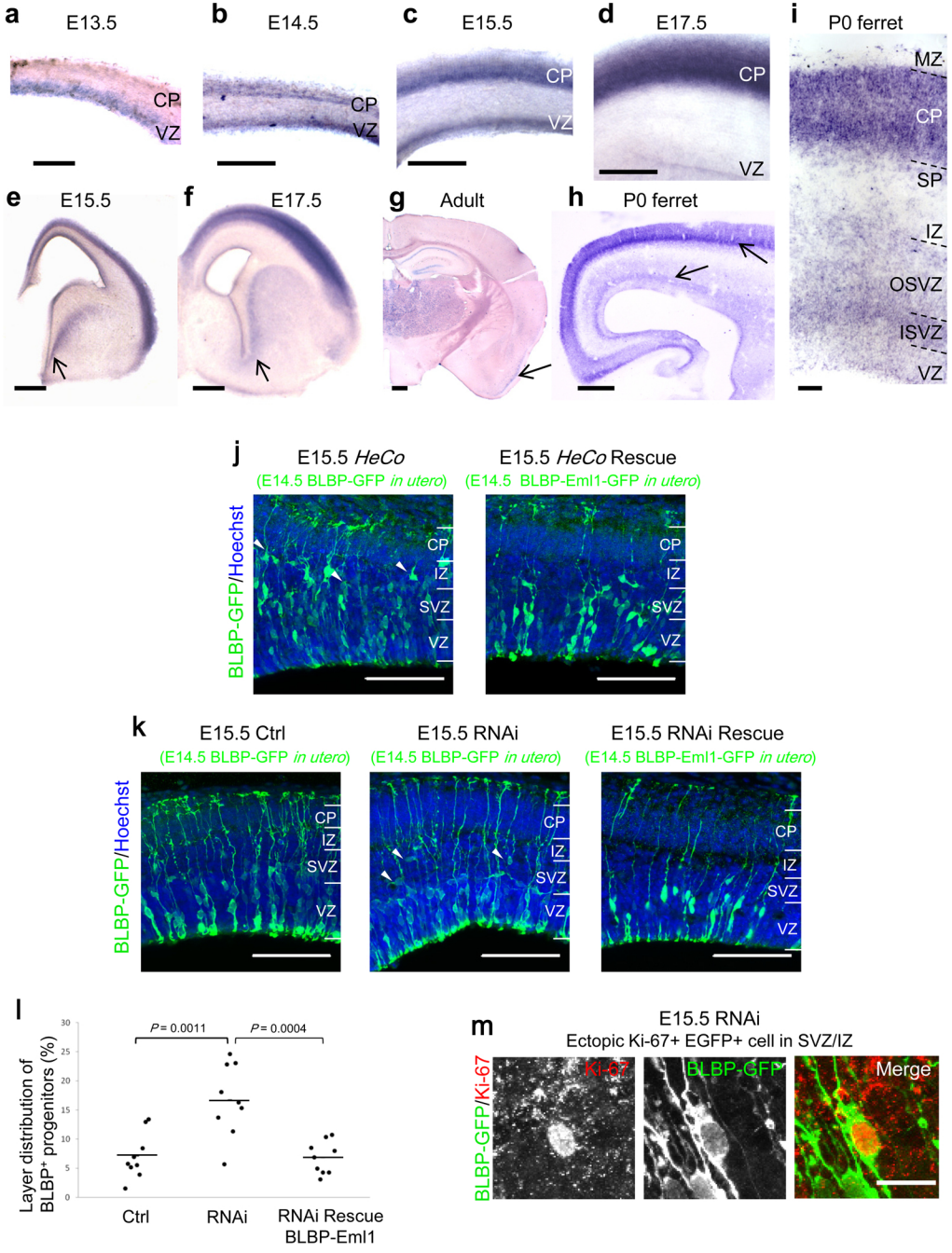
a
E13.5
CP
VZ
b
E14.5
CP
VZ
c
E15.5
CP
VZ
d
E17.5
CP
VZ
i
P0 ferret
MZ
CP
SP
IZ
OSVZ
ISVZ
VZ
e
E15.5
f
E17.5
g
Adult
h
P0 ferret
j
E15.5 HeCo
(E14.5 BLBP-GFP in utero)
E15.5 HeCo Rescue
(E14.5 BLBP-Eml1-GFP in utero)
BLBP-GFP/Hoechst
CP
IZ
SVZ
VZ
k
E15.5 Ctrl
(E14.5 BLBP-GFP in utero)
E15.5 RNAi
(E14.5 BLBP-GFP in utero)
E15.5 RNAi Rescue
(E14.5 BLBP-Eml1-GFP in utero)
BLBP-GFP/Hoechst
CP
IZ
SVZ
VZ
l
P = 0.0011
P = 0.0004
Layer distribution of BLBP+ progenitors (%)
30
25
20
15
10
5
0
Ctrl
RNAi
RNAi Rescue BLBP-Eml1
m
E15.5 RNAi
Ectopic Ki-67+ EGFP+ cell in SVZ/IZ
BLBP-GFP/Ki-67
Ki-67
BLBP-GFP
Merge

Figure 5

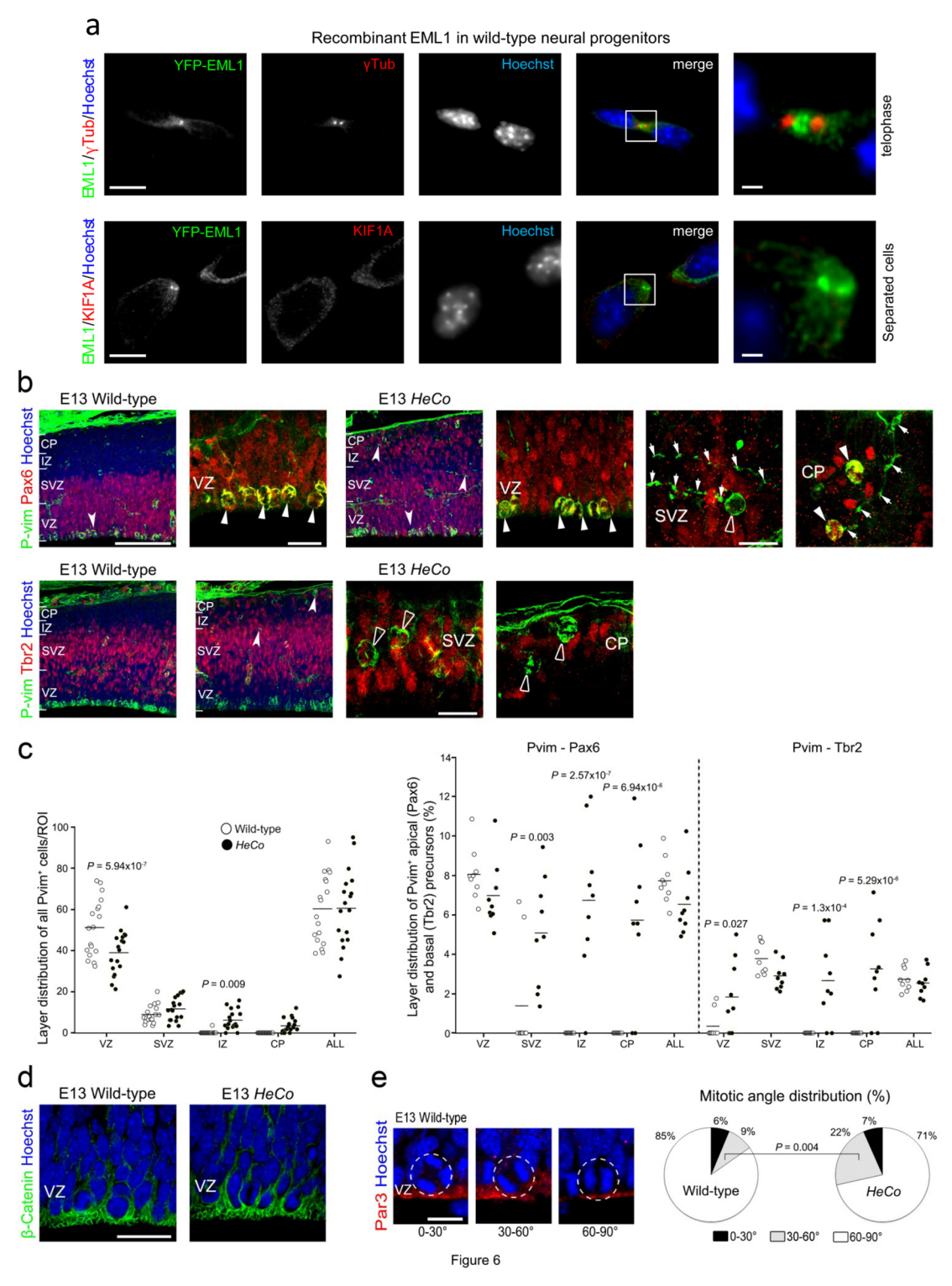
a
Recombinant EML1 in wild-type neural progenitors
EML1/γTub/Hoechst
YFP-EML1
γTub
Hoechst
merge
telophase
EML1/KIF1A/Hoechst
YFP-EML1
KIF1A
Hoechst
merge
Separated cells
b
E13 Wild-type
E13 HeCo
P-vim Pax6 Hoechst
CP
IZ
SVZ
VZ
P-vim Tbr2 Hoechst
c
Pvim - Pax6
Pvim - Tbr2
Wild-type
HeCo
Layer distribution of all Pvim+ cells/ROI
Layer distribution of Pvim+ apical (Pax6) and basal (Tbr2) precursors (%)
P = 5.94x10-7
P = 0.009
P = 0.003
P = 2.57x10-7
P = 6.94x10-6
P = 0.027
P = 1.3x10-4
P = 5.29x10-6
VZ
SVZ
IZ
CP
ALL
d
E13 Wild-type
E13 HeCo
β-Catenin Hoechst
e
E13 Wild-type
Par3 Hoechst
0-30°
30-60°
60-90°
Mitotic angle distribution (%)
85%
6%
9%
22%
7%
71%
P = 0.004
Wild-type
HeCo
0-30°
30-60°
60-90°

Figure 6

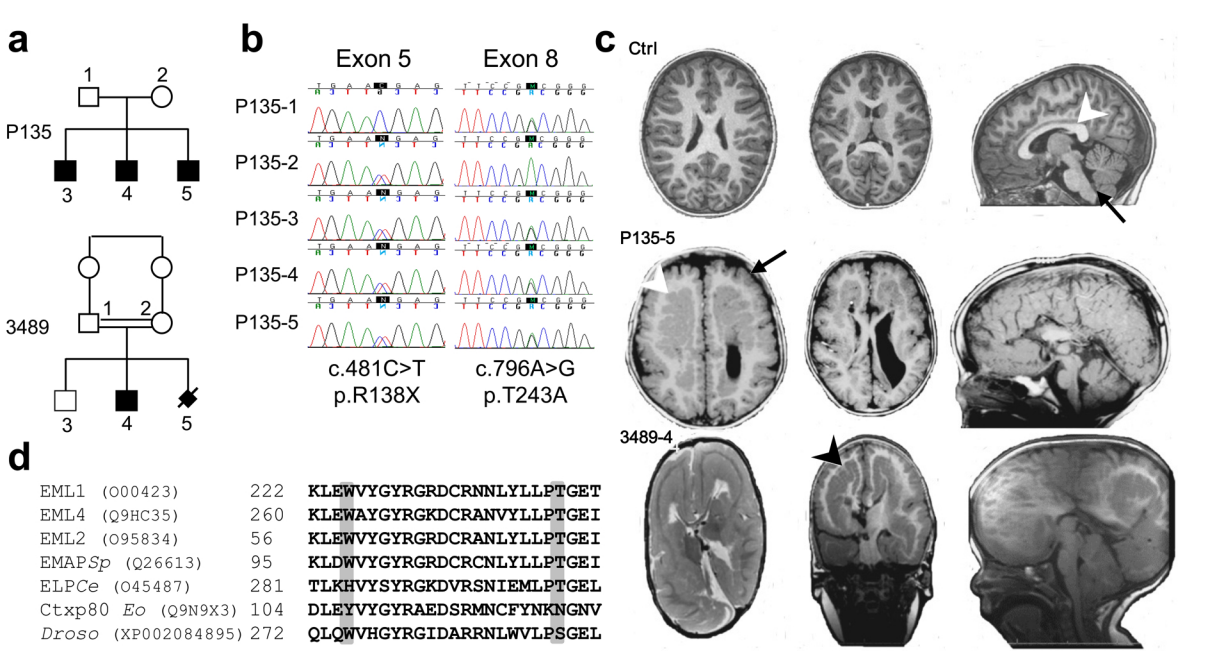
a
1
2
P135
3
4
5
1
2
3489
3
4
5
b
Exon 5
Exon 8
P135-1
P135-2
P135-3
P135-4
P135-5
c.481C>T
p.R138X
c.796A>G
p.T243A
c
Ctrl
P135-5
3489-4
d
EML1 (O00423) 222 KLEWVYGYRGRDCRNNLYLLPTGET
EML4 (Q9HC35) 260 KLEWAYGYRGKDCRANVYLLPTGEI
EML2 (O95834) 56 KLEWVYGYRGRDCRANLYLLPTGEI
EMAP*Sp* (Q26613) 95 KLDWVYGYRGRDCRCNLYLLPTGEI
ELP*Ce* (O45487) 281 TLKHVYSYRGKDVRSNIEMLPTGEL
Ctxp80 *Eo* (Q9N9X3) 104 DLEYVYGYRAEDSRMNCFYNKNGNV
Droso (XP002084895) 272 QLQWVHGYRGIDARRNLWVLPSGEL

Figure 7

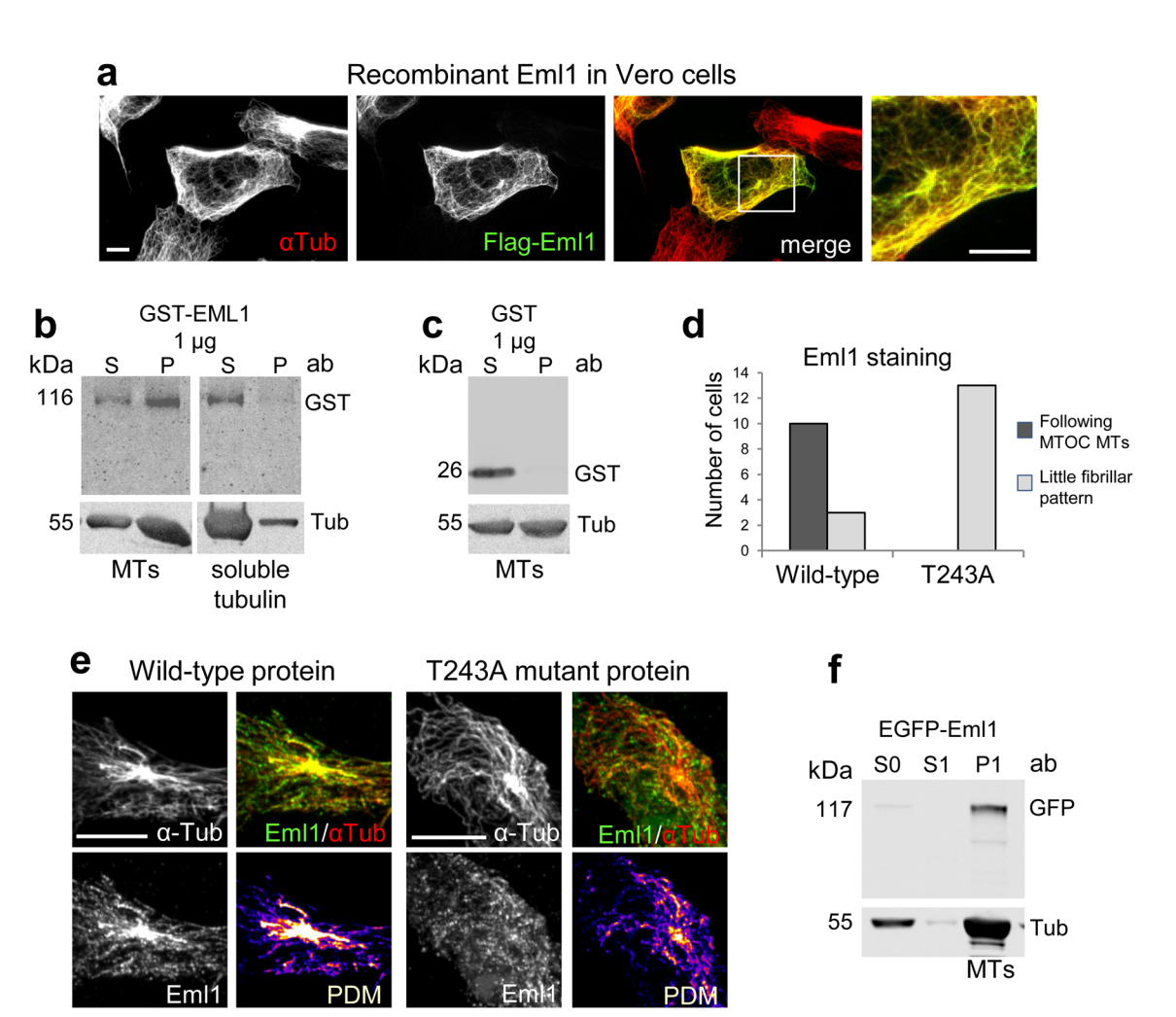
a
Recombinant Eml1 in Vero cells
αTub
Flag-Eml1
merge
b
GST-EML1
1 µg
kDa
S
P
S
P
ab
116
GST
55
Tub
MTs
soluble tubulin
c
GST
1 µg
kDa
S
P
ab
26
GST
55
Tub
MTs
d
Eml1 staining
Number of cells
0
2
4
6
8
10
12
14
Following MTOC MTs
Little fibrillar pattern
Wild-type
T243A
e
Wild-type protein
T243A mutant protein
α-Tub
Eml1/αTub
α-Tub
Eml1/αTub
Eml1
PDM
Eml1
PDM
f
EGFP-Eml1
kDa
S0
S1
P1
ab
117
GFP
55
Tub
MTs

Figure 8